

# Methylation index of Overly Branched tetraether lipids (MOB): a proxy for deep ocean (de)oxygenation?

Ronnakrit Rattanasriampaipong<sup>1</sup>, Yi Ge Zhang<sup>2</sup>, Olawale Alo<sup>3</sup>, Xiaolei Liu<sup>4</sup>, Yang Zhang<sup>5</sup>, Bumsoo Kim<sup>6</sup>, Franco Marcantonio<sup>7</sup>, Franck Bassinot<sup>8</sup>, and Tiegang Li<sup>9</sup>

<sup>1</sup>University of Arizona

<sup>2</sup>Guangzhou Institute of Chemistry

<sup>3</sup>The University of Oklahoma

<sup>4</sup>University of Oklahoma

<sup>5</sup>Ocean University of China

<sup>6</sup>Brown University

<sup>7</sup>Texas A&M University

<sup>8</sup>Laboratoire des Sciences du Climat et de l'Environnement

<sup>9</sup>First Institute of Oceanography, Ministry of Natural Resources, China

April 26, 2024

## Abstract

Branched glycerol dialkyl glycerol tetraethers (brGDGTs) with lower (sparsely-branched; SB-) and higher (overly-branched; OB-) numbers of methylated branches relative to the “regular” brGDGTs (B-GDGTs) are abundant in anoxic waters in the Black Sea. Observed changes in abundances and numbers of methylated branches of the entire series OB-GDGTs, B-GDGTs, and SB-GDGTs relative to dissolved oxygen (DO) levels in anoxic waters suggest that these compounds can potentially track changes in oceanic DO levels through time. To explore this, we determine the entire brGDGT series in surface or near-surface sediments from sites with different DO distributions in marine waters and sediments, extending the limited core-top collection of these lipids. We propose a modified methylation index based on only OB-GDGTs, called MOB, to avoid the potential impacts of terrestrial-derived B-GDGTs. Interestingly, MOB values in our extended core-top collection are strongly related to changes in bottom-water DO concentrations rather than the site-specific minimum DO values, i.e. usually within mid-depth oxygen minimum zones (OMZs). This suggests that sedimentary lipids are likely derived from heterotrophic bacteria living at the sediment-water boundary in sediments while lipids produced within mid-depth OMZs are not effectively exported to deep oceans. Analysis of MOB values in ancient sediments in the East Equatorial Pacific shows a gradual decline in bottom water DO, correlating with the progressive increase in global export productivity, organic carbon burial, and elevated level of deep-water nutrient contents since the middle Miocene. These findings highlight the potential of MOB as a tool for reconstructing past oceanic (de)oxygenation events.

Abstract content goes hereBranched glycerol dialkyl glycerol tetraethers (brGDGTs) with lower (sparsely-branched; SB-) and higher (overly-branched; OB-) numbers of methylated branches relative to the “regular” brGDGTs (B-GDGTs) are abundant in anoxic waters in the Black Sea. Observed changes in abundances and numbers of methylated branches of the entire series OB-GDGTs, B-GDGTs, and SB-GDGTs relative to dissolved oxygen (DO) levels in anoxic waters suggest that these compounds can potentially track changes in oceanic DO levels through time. To explore this, we determine the entire brGDGT series in surface or near-surface sediments from sites with different DO distributions in marine waters and sediments, extending the limited core-top collection of these lipids. We propose a modified methylation index based on only OB-

GDGTs, called MOB, to avoid the potential impacts of terrestrial-derived B-GDGTs. Interestingly, MOB values in our extended core-top collection are strongly related to changes in bottom-water DO concentrations rather than the site-specific minimum DO values, i.e. usually within mid-depth oxygen minimum zones (OMZs). This suggests that sedimentary lipids are likely derived from heterotrophic bacteria living at the sediment-water boundary in sediments while lipids produced within mid-depth OMZs are not effectively exported to deep oceans. Analysis of MOB values in ancient sediments in the East Equatorial Pacific shows a gradual decline in bottom water DO, correlating with the progressive increase in global export productivity, organic carbon burial, and elevated level of deep-water nutrient contents since the middle Miocene. These findings highlight the potential of MOB as a tool for reconstructing past oceanic (de)oxygenation events.

1 **Methylation index of Overly Branched tetraether lipids (MOB): a proxy for deep**  
2 **ocean (de)oxygenation?**

3 **Ronnakrit Rattanasriampaipong<sup>1,2,3\*</sup>, Yi Ge Zhang<sup>1,4\*</sup>, Olawale Alo<sup>5</sup>, Xiao-Lei Liu<sup>5</sup>, Yang**  
4 **Zhang<sup>1,6</sup>, Bumsoo Kim<sup>1,7</sup>, Franco Marcantonio<sup>8</sup>, Franck Bassinot<sup>9</sup> and Tiegang Li<sup>10</sup>**

5 <sup>1</sup>Department of Oceanography, Texas A&M University, College Station, TX, USA

6 <sup>2</sup>Department of Geosciences, The University of Arizona, Tucson, AZ, USA

7 <sup>3</sup>University Corporation for Atmospheric Research, Boulder, CO, USA

8 <sup>4</sup>State Key Laboratory for Isotope Geochemistry, Guangzhou Institute of Geochemistry, Chinese Academy of  
9 Sciences, Guangzhou, China

10 <sup>5</sup>School of Geosciences, The University of Oklahoma, Norman, OK, USA

11 <sup>6</sup>Frontiers Science Center for Deep Ocean Multispheres and Earth System, Key Lab of Submarine Geosciences and  
12 Prospecting Techniques, and College of Marine Geosciences, Ocean University of China, Qingdao, Shandong, China

13 <sup>7</sup>Department of Earth, Environmental and Planetary Sciences, Brown University, Providence, RI, USA

14 <sup>8</sup>Department of Geology & Geophysics, Texas A&M University, College Station, TX, USA

15 <sup>9</sup>Laboratoire des Sciences Du Climat et de L'Environnement, LSCE/IPSL, CEA-CNRS-UVSQ Université Paris-  
16 Saclay, Gif-sur-Yvette, Île-de-France, France

17 <sup>10</sup>Key Laboratory of Marine Sedimentology and Metallogeny, First Institute of Oceanography, Ministry of Natural  
18 Resources, Qingdao, China

19

20 \*Corresponding author(s):

21 Ronnakrit Rattanasriampaipong ([rrattan@ucar.edu](mailto:rrattan@ucar.edu)) and Yi Ge Zhang ([zhangyige@gig.ac.cn](mailto:zhangyige@gig.ac.cn))

22 Postal address: 1040 E 4th St, Tucson, AZ 85721

23

24 **Key Points**

- 25       • We investigated surface and downcore marine sediments with a focus on overly and  
26       sparsely branched GDGTs.
- 27       • Degrees of methylation index of overly branched GDGTs strongly correlate to bottom  
28       water oxygen concentrations.
- 29       • The bottom ocean appears to be losing O<sub>2</sub> since the late Miocene, coupled with increasing  
30       export productivity and deep-water nutrient levels.  
31

32 **Abstract**

33 Branched glycerol dialkyl glycerol tetraethers (brGDGTs) with lower (sparsely-branched; SB-)  
34 and higher (overly-branched; OB-) numbers of methylated branches relative to the “regular”  
35 brGDGTs (B-GDGTs) are abundant in anoxic waters in the Black Sea. Observed changes in  
36 abundances and numbers of methylated branches of the entire series OB-GDGTs, B-GDGTs, and  
37 SB-GDGTs relative to dissolved oxygen (DO) levels in anoxic waters suggest that these  
38 compounds can potentially track changes in oceanic DO levels through time. To explore this, we  
39 determine the entire brGDGT series in surface or near-surface sediments from sites with different  
40 DO distributions in marine waters and sediments, extending the limited core-top collection of these  
41 lipids. We propose a modified methylation index based on only OB-GDGTs, called MOB, to avoid  
42 the potential impacts of terrestrial-derived B-GDGTs. Interestingly, MOB values in our extended  
43 core-top collection are strongly related to changes in bottom-water DO concentrations rather than  
44 the site-specific minimum DO values, i.e. usually within mid-depth oxygen minimum zones  
45 (OMZs). This suggests that sedimentary lipids are likely derived from heterotrophic bacteria living  
46 at the sediment-water boundary in sediments while lipids produced within mid-depth OMZs are  
47 not effectively exported to deep oceans. Analysis of MOB values in ancient sediments in the East  
48 Equatorial Pacific shows a gradual decline in bottom water DO, correlating with the progressive  
49 increase in global export productivity, organic carbon burial, and elevated level of deep-water  
50 nutrient contents since the middle Miocene. These findings highlight the potential of MOB as a  
51 tool for reconstructing past oceanic (de)oxygenation events.

52 **Keywords:** bacterial tetraether lipids, dissolved oxygen, ocean (de)oxygenation, GDGTs,  
53 methylation index, MOB

54

55 **Plain Language Summary**

56 Membrane-spanning tetraether lipids of microbial organisms preserved in marine  
57 sediments, also known as “molecular fossils,” have been widely used as geochemical proxies to  
58 infer environmental changes in the past. Overly branched and sparsely branched tetraether lipids  
59 are new classes of organic compounds that have recently been identified and found to be abundant  
60 in marine waters where oxygen levels are low. Despite its potential as an oxygen indicator in past  
61 oceans, only a few studies have determined these lipids in modern marine sediments. Here, we  
62 analyzed these lipids from surface marine sediments collected from various locations with  
63 different oxygen levels in the water and found a strong link between the presence of these branched  
64 lipids and the amount of dissolved oxygen in deep oceans. This suggests that microbes in surface  
65 marine sediments are likely the main source of these new types of lipids. With new information  
66 from this work, we propose a new proxy that can track changes in deep ocean oxygen  
67 concentrations Earth’s history.

68

## 69 **1 Introduction**

70 Dissolved oxygen (DO) in the ocean is essential to all aerobic life. Instrumental records  
71 dating back to the 1960s confirm that DO concentrations in global oceans are declining in response  
72 to anthropogenic climate change (Cooley et al., 2022). The expansion of marine oxygen minimum  
73 zones (OMZ) in the tropics, such as in the Eastern Pacific Ocean, is one primary concern regarding  
74 oceanic changes in response to the ongoing deoxygenation (Busecke et al., 2022). Low DO levels  
75 in marine waters are harmful to marine life and can enhance the production of nitrous oxide, a  
76 potent greenhouse gas and a predominant ozone-depleting agent (Arévalo-Martínez et al., 2015; Ji  
77 et al., 2018). Moreover, the rise in numbers of hypoxic areas associated in human-induced factors,  
78 e.g. nutrient release, have been observed in lakes and coastal waters (Breitburg et al., 2018; Jenny  
79 et al., 2016). In global oceans, well-known marine regions with strong mid-depth OMZs are the  
80 Eastern Tropical Pacific Ocean, the Black Sea, and the Arabian Sea (Boxes 2, 3, and 4 in Fig. 1A).  
81 Because of the intrinsic interplay among various factors affecting marine OMZ regions, Earth  
82 system models have yet to provide a consistent projection of how these marine OMZs will change  
83 (cf. Busecke et al., 2022; Cabré et al., 2015). The reconstruction of past DO levels based on  
84 geochemical proxies offers an independent view that helps to understand marine OMZs in a  
85 warming world.

86 Quantifying levels of oxygen concentrations in paleo-oceans is typically complex and  
87 problematic due to the complexity of interplays across physical, chemical, and biological  
88 processes. Most geochemical proxies are linked to chemical cycling of nitrogen, sulfur, and carbon  
89 that are sensitive to redox conditions, from which past oxygen conditions are qualitatively inferred.  
90 Only a few geochemical and/or paleontological proxies have been quantitatively calibrated to DO  
91 levels in seawater. Examples of proxies that indirectly reflect changes in oxygen levels in seawater  
92 include but are not limited to, (i) concentrations of redox-sensitive trace metals, such as vanadium  
93 (V), uranium (U), molybdenum (Mo), and rhenium (Re), in sediments (Bennett and Canfield,  
94 2020; Tribovillard et al., 2006), (ii) stable isotopic signatures of organic nitrogen ( $\delta^{15}\text{N}$ ) bound in  
95 foraminiferal tests (cf. Auderset et al., 2019; Hess et al., 2023; Wang et al., 2022), and (iii) the  
96 ratio of trace elements incorporated to foraminiferal calcite to calcium, such as Mn/Ca (Barras et  
97 al., 2018) and I/Ca (Glock et al., 2014; Lu et al., 2020; Zhou et al., 2014). Porosity and pore density

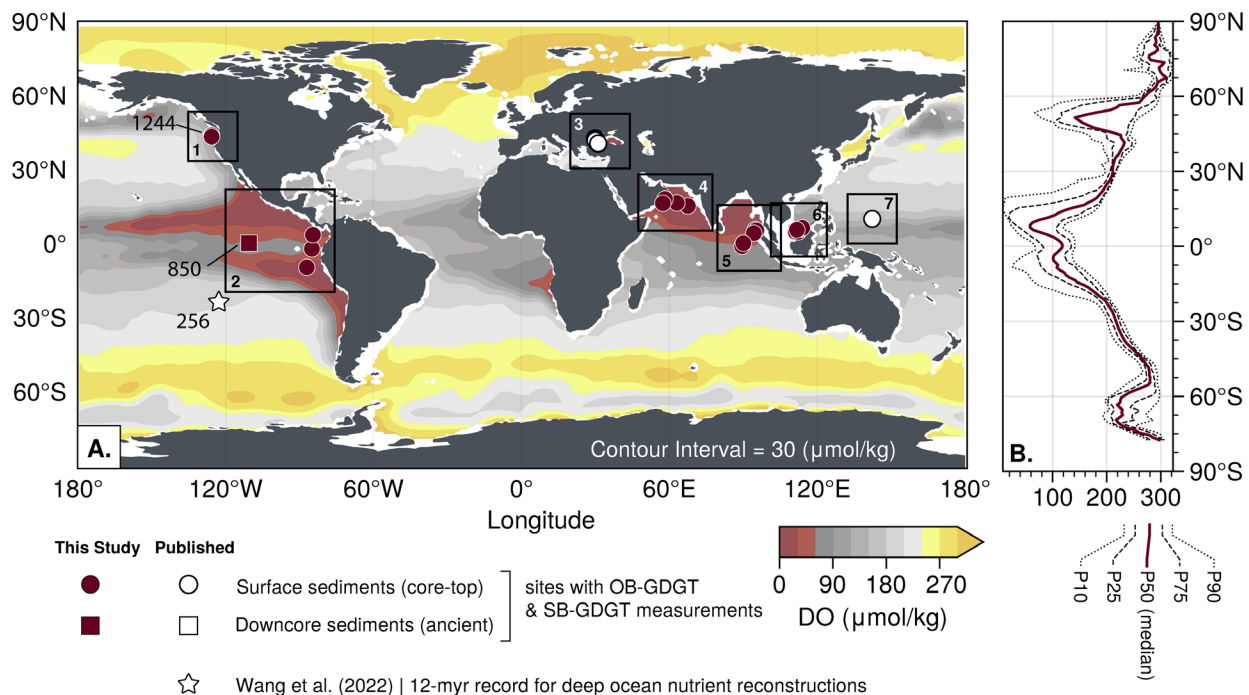


**Fig. 1. Location of sites discussed in this study overlaid on the spatial distribution of dissolved oxygen concentrations at the 200-m depth level.** (A) The map shows the modern locations of the study sites in our expanded data set. Tetraether lipids discussed in this paper were extracted and derived from surface sediments and down-core sediments. Sites with new GDGT measurements from this study are colored in maroon. Sites with published GDGT data are colored in white. The data set covers eight different marine regions, including (1) Pacific NW (Cascadia Margin), (2) Eastern Equatorial Pacific (EEP), (3) Western Tropical North Atlantic (WTNA) (Liu et al., 2014) (4) Black Sea (Liu et al., 2014), (5) Arabian Sea, (6) Eastern Equatorial Indian Ocean (EEIO), (7) South China Sea (SCS), and (8) Mariana Trench (Zeng et al., 2023). Shaded contours (Contour Interval "C.I." = 30) show the distribution of dissolved oxygen (DO) at 200-m water depth based on the 2018 World Ocean Atlas (WOA18) database ( $1^\circ \times 1^\circ$  spatial resolution). The shades of red indicate low oxygen conditions ( $<60 \mu\text{mol/kg}$  of seawater DO) (B) Latitudinal means of the 200-m WOA18 DO are also presented with P10, P25, P75, and P90 DO values.

98 of foraminifera is likely the only proxy that has evolved from a qualitative to a quantitative proxy  
 99 (Glock et al., 2011; Rathburn et al., 2018). A quantitative organic proxy for DO levels in seawater  
 100 has rarely been established.

101 Branched glycerol dialkyl glycerol tetraethers (brGDGT) are membrane-spanning lipids  
 102 that were initially identified in samples from peatlands (Sinninghe Damsté et al., 2000) but later  
 103 found to be ubiquitous in several environmental settings, including soils (e.g., Weijers et al., 2007),  
 104 rivers (De Jonge et al., 2014; Zell et al., 2013), lakes (e.g., Buckles et al., 2014; Tierney and  
 105 Russell, 2009), groundwaters (e.g., Ding et al., 2018), hydrothermal vents (e.g., Li et al., 2018),  
 106 marine waters (e.g., Xie et al., 2014), and ocean sediments (e.g., Liu et al., 2012). The core

107 structures of brGDGT are ether-linked glycerol lipids with varying numbers of methylated  
108 branches and internal cyclopentane rings. The original determination of the chemical structures of  
109 “regular” brGDGT, hereafter B-GDGT, shows that the internal biphytanyl skeletons have 4–6  
110 methyl branches and can contain up to two cyclopentyl moieties (Weijers et al., 2006b, 2007) (Fig.  
111 2). Although the chemical structures of brGDGTs are similar to membrane-spanning isoprenoidal  
112 GDGT (isoGDGT) synthesized by marine Archaea, the stereochemical configuration of brGDGTs  
113 suggests bacterial sources (Weijers et al., 2006a).

114 Empirical observation of brGDGTs in natural archives shows that their compositional  
115 distributions are strongly correlated with environmental temperature and soil pH, which form the  
116 basis for several brGDGT-based environmental proxies (cf. Martínez-Sosa et al., 2021; Peterse et  
117 al., 2012; Raberg et al., 2023; Weijers et al., 2007). In marine settings, B-GDGT is generally low  
118 in abundance. Elevated concentrations of B-GDGT in marine sediments are typically assumed to  
119 be derived from terrestrial sources, as expressed by high values of the Branched versus Isoprenoid  
120 tetraether (BIT) index (Hopmans et al., 2004; Huguet et al., 2007). However, recent culture studies  
121 of a few known strains of *Acidobacteria* show that they synthesize brGDGTs in response to  
122 oxygen-limiting conditions (Chen et al., 2022; Halamka et al., 2023, 2021), suggesting that marine  
123 microbes that thrive in DO-stress environments may synthesize brGDGTs. As described by (Liu  
124 et al., 2012), two new brGDGT subclasses with relatively higher (overly branched; OB-) and lower  
125 (sparsely branched; SB-) numbers of methyl branches along glycerol backbones than the B-GDGT  
126 subclass (Fig. 2) have been found to be abundant in low DO marine waters from the Eastern  
127 Tropical North Pacific (Xie et al., 2014), the Black Sea, and the Cariaco Basin (Liu et al., 2014).  
128 They are also abundant in core-top sediments from the Black Sea (Liu et al., 2014). This collection  
129 of samples with the entire series of brGDGTs shows that concentrations of non-cycloalkylated  
130 brGDGTs and the degree of brGDGT methylation—as expressed by the Methylation Index of OB-  
131 GDGT, B-GDGT, and SB-GDGT ( $MI_{OB/B/SB}$ )—increase when DO levels decrease (Liu et al.,  
132 2014). Notably, the presence of OB-GDGT in ancient marine sediments deposited during Oceanic  
133 Anoxic Event 2 (OAE2; circa 94 Ma) suggests that these new subclasses of brGDGTs can be  
134 preserved in marine sediments for millions of years (Connock et al., 2022) and are likely related  
135 to low DO conditions in marine environments.

## Branched GDGTs (B-GDGTs)

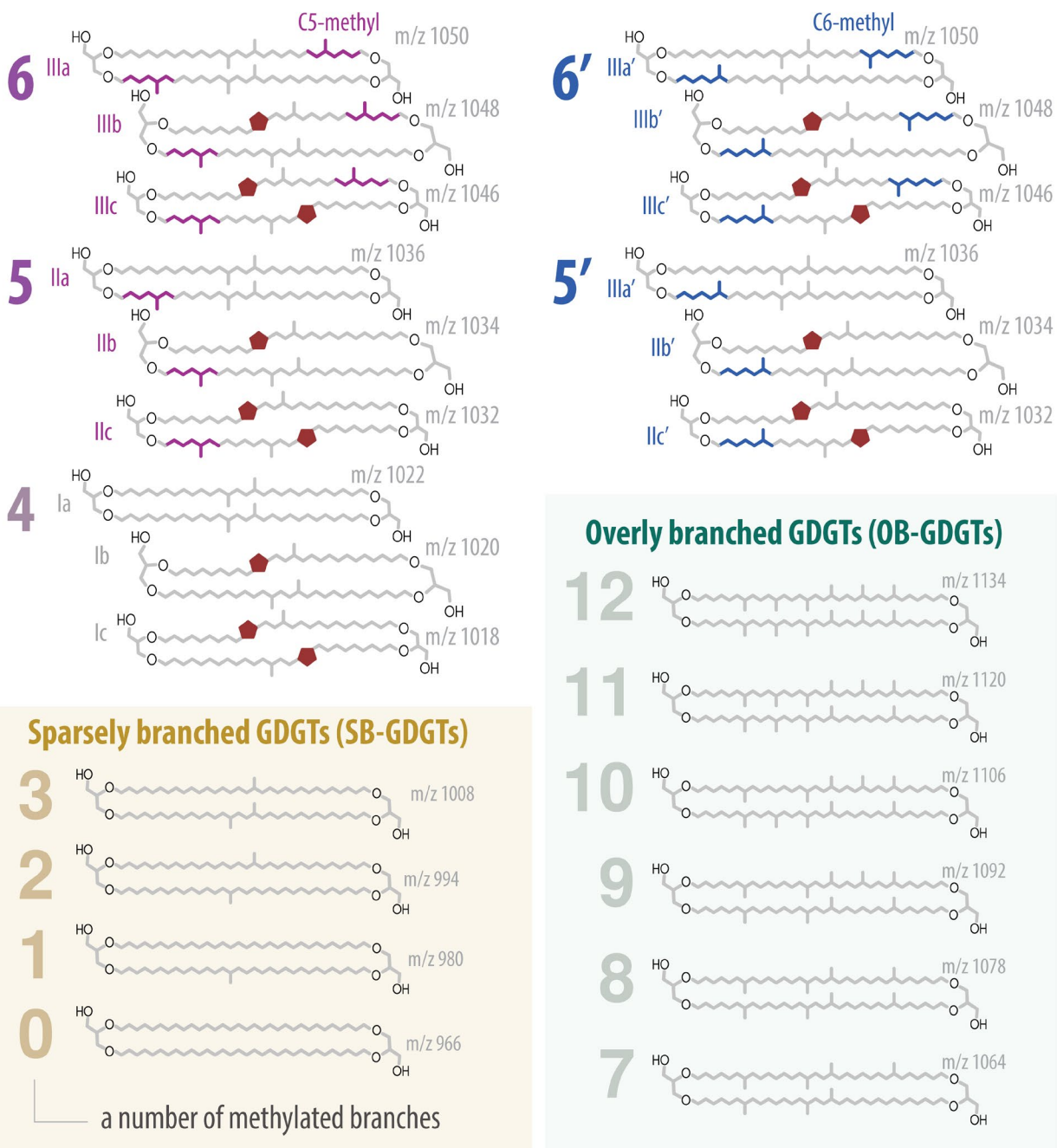


**Fig. 2. Structures of tetraether lipids discussed in this study.** Three main groups of non-isoprenoid branched glycerol dialkyl glycerol tetraethers (brGDGTs) discussed in this study are (1) regular branched GDGTs (B-GDGTs), (2) derivatives with fewer methylated branches, called sparsely-branched GDGTs (SB-GDGTs), and (3) derivatives with a higher number of methylated branches, called overly-branched GDGTs (OB-GDGTs). Mass-to-charge ( $m/z$ ) ratios for each molecule are labeled on the upper right. The numbers labeled in front of each molecule represent a varying number of methylated branches. For B-GDGTs, structures for C5-methylated (left column) and C6-methylated (right column) B-GDGTs are shown separately.

137 Despite its great potential to be a proxy for marine (de)oxygenation, it is still unclear  
138 whether sedimentary OB-GDGT and SB-GDGT are mainly derived from mid-depth OMZs in  
139 open oceans. As recognized by Xie et al. (2014), suspended particulate matter (SPM) from depths  
140 below the OMZ in the Eastern Tropical North Pacific show low concentrations of the OB-GDGT  
141 and SB-GDGT fractions, indicating that (i) DO level in the OMZ is not low enough to trigger  
142 massive production of these lipids and/or (ii) there is no effective export mechanisms at  
143 intermediate water depths. Zeng et al. (2023) also recently investigated the distribution of brGDGT  
144 lipids in seafloor sediments from the Mariana Trench and have argued that relatively high  
145 abundances of OB-GDGT and SB-GDGT are synthesized by *unclassified* anaerobic bacterial  
146 communities in marine sediments unique to the hadal oceans. Although OB-GDGT and SB-GDGT  
147 in marine sediments were first described more than a decade ago (Liu et al., 2012), only a few  
148 studies reported these lipids in marine waters and sediments, making it difficult to evaluate the  
149 sources and their distributions in marine sediments fully.

150 Here, we report the distributions of the entire series of brGDGTs in surface marine  
151 sediments from five different regions, expanding the collection of existing published OB-GDGT  
152 and SB-GDGT data (**Fig. 1**). Alongside the down-core analysis, our aim is to identify the oxygen  
153 levels at which depths become the dominant controlling factor of the distribution of these  
154 brGDGTs. We further investigate the potential of the degree of methylation of OB-GDGTs as a  
155 quantitative organic geochemical proxy for past marine (de)oxygenation.

## 156 **2 Materials and Methods**

### 157 **2.1 Data compilation and materials**

158 Measurements of tetraether lipids with OB-GDGT and SB-GDGT fractions ( $n = 67$ ) were  
159 compiled from four publications, and newly conducted by this study (see **Table 1**). This study  
160 determined fractional abundances of tetraether lipids extracted from the core-top ( $n = 24$ ), near-  
161 surface ( $n = 4$ ), and ancient marine sediments ( $n = 23$ ). These data have expanded the spatial  
162 coverage of sites with OB-GDGT and SB-GDGT measurements spanning a wide range of vertical  
163 DO distributions in modern oceans (see **Figs. 1 and 3**). We grouped the based on their geographical  
164 distributions as follows: (1) Pacific Northwest, (2) Eastern Equatorial Pacific (EEP), (3) Black  
165 Sea, (4) Arabian Sea, (5) East Equatorial Indian Ocean (EEIO), (6) South China

**Table 1.** Information for study sites with GDGT measurements

	<b>Region</b>	<b>Data Type</b>	<b>Cruise/Site</b>	<b>Source</b>	<b>Count</b>
1	Pacific Northwest (Cascadian Ridge)	Near-surface	ODP 1244	This study	3
2	Eastern Equatorial Pacific (EEP)	Core top	MV1014_xx	This study	4
		Near-surface	ODP 850	This study	1
		Ancient	ODP 850	This study	23
3	Black Sea	Core top	BS_GeoB7xx	<a href="#">Liu et al. (2014)</a>	12
4	Arabian Sea	Core top	MD77-2xx	This study	6
5	Eastern Equatorial Indian Ocean (EEIO)	Core top	BAR94-2x, MD77-159/160	This study	8
6	South China Sea (SCS)	Core top	WPxx	This study	6
7	Mariana Trench	Core top	MT03	<a href="#">Zeng et al. (2023)</a>	4
				<b>Total</b>	<b>67</b>

166 Sea (SCS), and (7) Mariana Trench (see **Fig. 1**).

167 *2.2.1 Surface and near surface marine sediments*

168 For core-top GDGT samples, Eastern equatorial Pacific multi-corer samples were collected  
169 aboard the R/V *Melville* in 2010 ([Marcantonio et al., 2014](#)). Samples MV1014\_01\_01\_MC  
170 (5°49.0863N, 85°44.528W; water depth 1760.4 m), MV1014\_02\_16\_MC (00°10.8297'S,  
171 85°52.0042'W; water depth 2846.0 m), and MV1014\_03\_20\_MC (08°30.001'S, 87°02.695'W;  
172 water depth 4407.0 m) were collected from near the Cocos Ridge, Carnegie Ridge, and Peru Basin,  
173 respectively. The Cocos and Carnegie Ridge samples were collected from the margins of the  
174 Panama Basin, with the Carnegie Ridge multi-corer samples retrieved from a highly productive  
175 site (sediment mass accumulation rate, MARs) of about 4 g·cm<sup>-2</sup>·kyr<sup>-1</sup>, and the Cocos Ridge multi-  
176 corer samplers from a site that was not as productive and had a lower MAR (0.3 g·cm<sup>-2</sup>·kyr<sup>-1</sup>)  
177 ([Marcantonio et al., 2014](#)). The Peru Basin multi-corer samples were collected within the South  
178 Pacific oligotrophic gyre, and MARs could not be measured. The Arabian Sea piston cores MD77-  
179 200 (16°33.0'N, 67°54.0'E; water depth 2910 m), MD77-201 (17°33.6'N, 63°5.4'E; water depth  
180 3665 m), MD77-204 (19°10.8'N, 58°15.6'E, water depth 1430 m), and MD77-205 (17°26.4'N,  
181 57°24.0'E; water depth 969 m) were collected aboard the R/V *Marion Dufresne* in 1977 from the

182 Arabian Sea during the OSIRIS 3 campaign (Jean-Claude, 1977). For EEIO, core-top samples  
183 were from two different expeditions. The first set of samples MD77-159 (0°4.2'N; water depth  
184 4241 m) and MD77-160 (1°15.0'N, 90°1.8'E; water depth 2160 m) were collected during the same  
185 cruise OSIRIS 3. The second set of samples BAR94-24 (6°44.4'N, 94°50.46'E; water depth 2676  
186 m), BAR94-25 (6°26.1'N, 95°19.5'E; water depth 1558 m), and BAR94-27 (5°20.4'N, 94°18.3'E;  
187 water depth 2689 m) were collected aboard R/V *Baruna Jaya I* during the 1994 BARAT campaign  
188 (Guichard and Hardjawidjaksana, 1994). For SCS, core-top samples WP01 (6°40.458'N,  
189 111°13.92'E; water depth 1848 m), WP02 (5°51.522'N, 111°14.094'E; water depth 1289 m),  
190 WP03 (5°52.146'N, 112°18.072'E; water depth 687 m), WP04 (6°55.704'N, 113°6.744'E; water  
191 depth 1569 m), WP05 (7°28.446'N, 113°54.852'E; water depth 913 m), and WP06 (6°41.01'N,  
192 111°45.534'E; water depth 1926 m) were collected aboard the R/V *Ke Xue Yi Hao* (formerly  
193 named *Kexue I*) during the South China Sea Survey Cruise in 2012.

194 We also investigate shallow down-core GDGT data with sampling depth shallower than  
195 10 meters, including samples from the Mariana Trench (Zeng et al., 2023), the EEP ODP Site 850,  
196 and the Cascadia Margin and treat them as shallow “core-top” samples to maximize the number  
197 of observations for the core-top data set and its spatial coverage. Given persistent low O<sub>2</sub>  
198 conditions in the Cascadian Ridge region since 32,000 years ago (cf. Saravanan et al., 2020),  
199 GDGT distributions of ODP Site 1244C down-core sediments dated ~30,000 years old are not  
200 expected to be very different from surface sediments (44°35.1702'N, 125°7.1902'W; modern  
201 water depth 895.1 m below sea level (mbsl); sampling depths ~7–8 m deep; see Fig. 1).

## 202 2.2.2 Lipid extracts derived from ancient marine sediments

203 For paleo-GDGT samples, we determined GDGT distributions from 24 polar lipid fractions  
204 derived from ancient sediments from the Ocean Drilling Program (ODP) Site 850 (1°17.838'N,  
205 110°31.284'W; modern water depth 3786.1 m; see Fig. 1). The samples selected for this study are  
206 a subset of the original data set used to reconstruct the SST history of EEP over the past 12 million  
207 years (Zhang et al., 2014).

## 208 2.2 Lipid analysis

### 209 2.2.1 Sample preparation

210 Total lipid extracts (TLEs) derived from surface, near-surface, and down-core marine  
211 sediments were prepared at Texas A&M University. Forty-one marine sediment samples (~0.5–  
212 13 g) were freeze-dried and homogenized with mortar and pestle. The grounded sediments were  
213 then subjected to lipid extraction using a Dionex 350 Accelerated Solvent Extractor (ASE) with  
214 9:1 (v/v) dichloromethane/methanol at 120°C and 10.34 MPa for five static cycles. Subsequently,  
215 the TLEs were dried in an ultrapure nitrogen stream and stored in 2 ml vials for subsequent  
216 analysis.

### 217 2.2.2 GDGT determination

218 GDGT determinations were performed at the University of Oklahoma. Sample preparation  
219 and analytical setup are modified after [Connock et al. \(2022\)](#). Each TLE sample was redissolved  
220 in 1 ml pure MeOH, ultrasonicated for 10 minutes, and centrifuged at 3000 rpm for five minutes.  
221 Following centrifugation, 500 µl of the TLE redissolved in MeOH were transferred into a 2 ml  
222 injection vial for lipid analysis. Reversed-phase high-performance liquid chromatography coupled  
223 to electrospray ionization quadrupole time-of-flight mass spectrometry (RP-HPLC-ESI-Q-TOF-  
224 MS) was performed with an Agilent 1290 series UPLC system coupled to an Agilent 6530 Q-TOF  
225 mass spectrometer through an Agilent jet stream dual electrospray ionization (AJS-ESI) interface.  
226 For each TLE sample, 10 µl out of the 500 µl volume were injected onto an ACE UltraCore Super  
227 C18 column (5 µm, 2.1 × 250 mm, ACE, Aberdeen, UK) maintained at 45 °C. Following method  
228 parameters were set to achieve the separation of GDGTs: (i) For Q-TOF, voltages of 3500 V, 175  
229 V, 65 V, 750 V were set for a capillary, a fragmentor, a skimmer, an octupole, respectively, in auto  
230 MS/MS scanning mode with MS range of m/z 50-2000 and MS/MS range of m/z 20-2000. (ii) For  
231 ESI, the drying gas (N<sub>2</sub>) temperature was set at 300 °C with the flow rate of 8 L min<sup>-1</sup> and the  
232 nebulizer gas (N<sub>2</sub>) pressure of 35 PSIG. For RP-HPLC, two eluents, A and B, were used. Eluent  
233 A was 95:5:0.04:0.10 of methanol/H<sub>2</sub>O/formic acid/14.8 M NH<sub>3</sub> (aq.), and eluent B was  
234 50:50:0.04:0.10 of hexane/2-propanol/formic acid/14.8 M NH<sub>3</sub> (aq.). A flow rate of 0.2 mL min<sup>-1</sup>,  
235 first hold 100% A for 5 min, and to 70% A and 30% B in 25 min, followed by a gradient to 50%  
236 B at 50 min and hold for 5 min, and finally re-equilibrated with 100% eluent A at a flow rate of  
237 0.4 mL min<sup>-1</sup> for 5 min. GDGTs were identified based on accurate masses, retention time, and  
238 diagnostic fragments. Quantification was achieved with an extraction window of [M+H]<sup>+</sup> being ±  
239 0.02 m/z units. We quantified relative abundances for four main subclasses of GDGT in all new

240 GDGT measurements, including isoGDGTs, B-GDGTs, OB-GDGTs, and SB-GDGTs, without  
241 separating C5- and C6-methyl derivatives.

## 242 **2.3 Dissolved Oxygen in Seawater for Modern GDGT Data**

### 243 *2.3.1 Site-specific DO vertical profiles*

244 Sampling sites of surface sediments with new GDGT measurements from this study have  
245 expanded from previously published works, representing a more comprehensive range of different  
246 DO distributions in water columns (see **Fig. 3**). We use objectively analyzed climatological mean  
247 fields of the DO data set (named *o\_an*; 1°x1° spatial resolution; 0–5500 meters at standard depth  
248 levels; 1900–2017) from the 2018 World Ocean Atlas (WOA18) database ([Garcia et al., 2019](#)) to  
249 determine different degrees of (de)oxygenation in the water column above each sampling site. We  
250 read the WOA18 DO data set (*NetCDF file*) using the *Xarray* Python library ([Hoyer and Hamman,](#)  
251 [2017](#)) to perform all the data manipulation and matching. The sampling coordinates (latitude,  
252 longitude) of the GDGT data were matched to the closest grid using the built-in *nearest* method.  
253 We limited the deepest depth of any matched WOA18 DO profiles using the sampling depth of  
254 the GDGT data. For the Mariana Trench core top data, we used the in situ measurements of DO  
255 collected during the descent of the cable of a conductivity-temperature-depth (CTD) device at the  
256 Challenger Deep of the Mariana Trench (11°22.569'N, 142°18.105'E; deepest sampling depth  
257 10000 m) in December 2015 ([Tian et al., 2018](#)) as the WOA18 DO data is unavailable for the  
258 entire water column. The location of the CTD cast at Challenger Deep is approximately 29  
259 kilometers from the MT3 core site ([cf. Zeng et al., 2023](#)), reasonably comparable to the 1°x1°  
260 spatial resolution of the WOA18 DO data set.

### 261 *2.3.2 DO-derived parameters reflecting different degrees of oxygenation in seawater*

262 To determine the position in the water column where the strongest response of brGDGT  
263 distributions to different degrees of oxygenation occur, we calculated parameters that reflect  
264 degrees of oxygenation at different locations and depth ranges in each DO vertical profile. **Fig. 4**  
265 shows an example DO vertical profile with annotated positions and depth ranges of DO-derived  
266 parameters, including ① *minOxy*, ② *insituOxy*, ③ *oxycline2oxymin*, ④ *normIntgOMZ*, ⑤  
267 *surface2insitu*, ⑥ *oxycline2insitu*, and ⑦ *OMZdepthRatio*. Three key depth levels needed for

268 the calculation of these parameters are (i) the *oxycline* depth, (ii) the *bottomOMZ* depth, and (iii)  
 269 the sampling depth (in situ depth). The fastest rate of declining DO concentrations from surface  
 270 defines the *oxycline* depth. The *bottomOMZ* depth is defined by the fastest rate of increase in the  
 271 DO concentration below the *oxycline* depth.

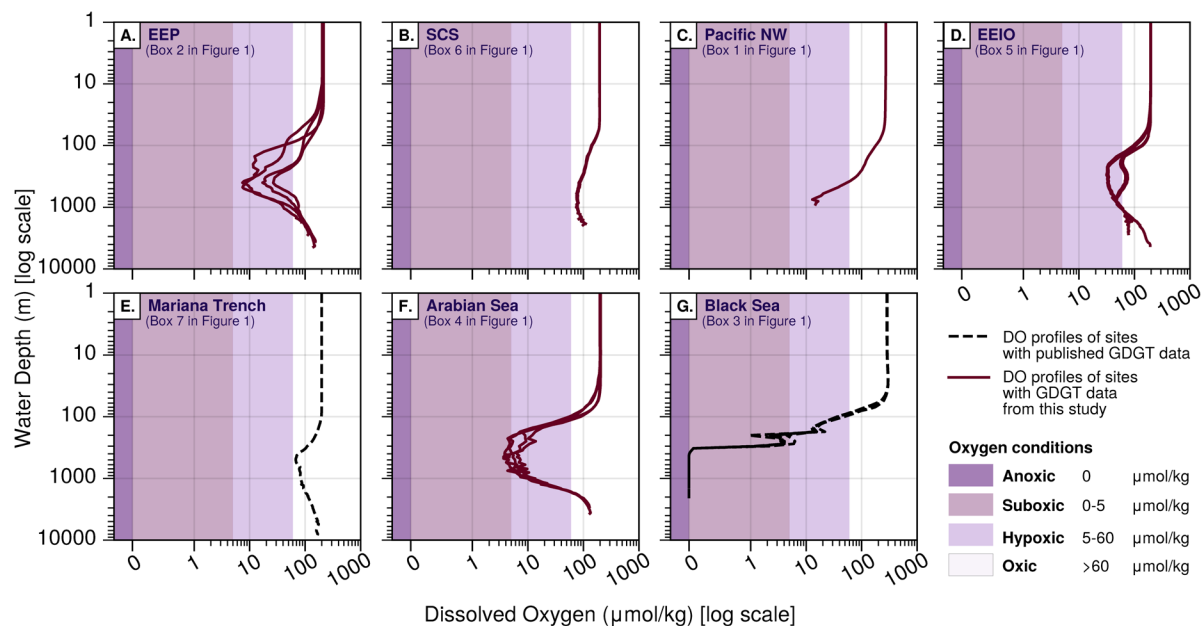


**Fig. 3. Overview of the vertical distributions of dissolved oxygen (DO) concentrations.** Each subplot shows the vertical DO distributions above surface sediment sampling sites at different regions shown in Fig. 1: (A) Eastern Equatorial Pacific (EEP), (B) South China Sea (SCS), (C) Pacific Northwest (Pacific NW), (D) Eastern Equatorial Indian Ocean (EEIO), (E) Mariana Trench, (F) Arabian Sea, and (G) Black Sea. Black dashed lines are DO profiles of sites with published GDGT data. Maroon solid lines are DO profiles of sites with GDGT data from this study. Shades of purples indicate different oxygen conditions: anoxic (0  $\mu\text{mol/kg}$ ; dark purple), suboxic (0–5  $\mu\text{mol/kg}$ ; purple), hypoxic (5–60  $\mu\text{mol/kg}$ ; pale purple), and oxidic (>60  $\mu\text{mol/kg}$ ; white).

## 272 3 Results and Discussion

### 273 3.1 Degree of methylation of brGDGTs at different oxygen conditions

274 The Methylation Index of OB-GDGT, B-GDGT, and SB-GDGT ( $\text{MI}_{\text{OB/B/SB}}$ ) has been  
 275 proposed by Liu et al. (2014) to track the changes in both fractional abundances and degrees of  
 276 methylation for the entire series of brGDGTs. To avoid confusion of the  $\text{MI}_{\text{OB/B/SB}}$  index with the  
 277 Methane Index (abbreviated as MI; Zhang et al., 2011), we propose the new abbreviation as “DMI”  
 278 (Degree of Methylation of brGDGTs Index). This new DMI abbreviation also differs from the  
 279 fractional abundance ratio of B-GDGTs with different methylated branches, i.e., the Methylation  
 280 of Branched Tetraethers (abbreviated as MBT; Weijers et al., 2007). The higher values of

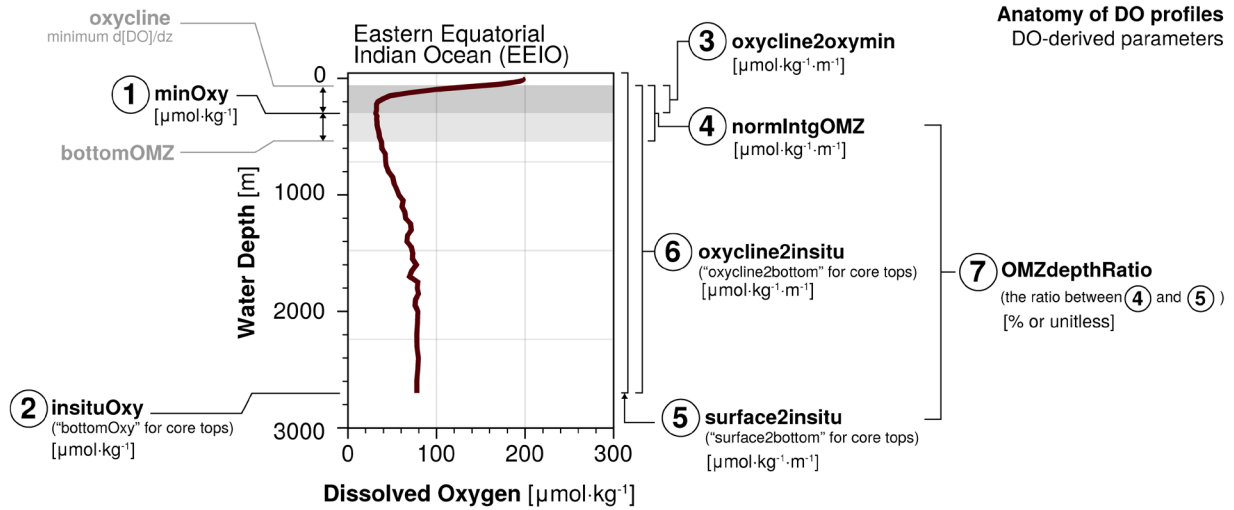


**Fig. 4. An example DO profile with annotations of DO-related parameters.** Seven different DO-related parameters were calculated from a site-specific DO vertical profile using the 2018 World Ocean Atlas database (Garcia et al., 2019).

281 DMI<sub>OB/B/SB</sub> reflect the distributional shift towards brGDGT structures with higher numbers of  
282 methylated branches. The equation of MI<sub>OB/B/SB</sub> is expressed as follows:

$$DMI_{OB/B/SB} = \frac{(\sum_{n=7}^{12} n * [X_{OB}]) + (\sum_{n=4}^6 n * [X_B]) + (\sum_{n=0}^3 n * [X_{SB}])}{[\Sigma OB + \Sigma B + \Sigma SB]} \quad (1)$$

283 where  $[X_{OB}]$ ,  $[X_B]$ , and  $[X_{SB}]$  represent fractional abundances for OB-GDGT, B-GDGT, and SB-  
284 GDGT, respectively, while  $n$  denotes the number of methylated branches of each GDGT fraction.  
285 If sedimentary OB-GDGT and SB-GDGT are derived primarily from the mid-depth OMZ in the  
286 water column, the value ranges of MI<sub>OB/B/SB</sub> of samples from places where strong OMZs exhibit  
287 in the water column ( $minOxy < 60 \mu\text{mol}\cdot\text{kg}^{-1}$  DO) should be higher and *significantly different* from  
288 places where mid-depth water are oxic ( $minOxy \geq 60 \mu\text{mol}\cdot\text{kg}^{-1}$  DO). Given the small sample size  
289 and non-Gaussian distribution in each data set, we chose the non-parametric Mann-Whitney U test  
290 (MWU; also called the Wilcoxon rank-sum test) to assess whether the medians between oxic and  
291 low oxygen data clusters differ *significantly*. The resulting  $p$  value ( $p < .01$ ) suggests that the  
292 medians of the two clusters are *significantly different* from each other; however, the value ranges  
293 between low oxygen and oxic clusters overlap in large part (Fig. 5A). It should be noted that new  
294 GDGT measurements from this study emphasize the distinction in the DMI<sub>OB/B/SB</sub> value ranges  
295 between low oxygen and oxic conditions compared to the clusters of the limited collection of  
296 published data (maroon versus gray dots in Fig. 5A).

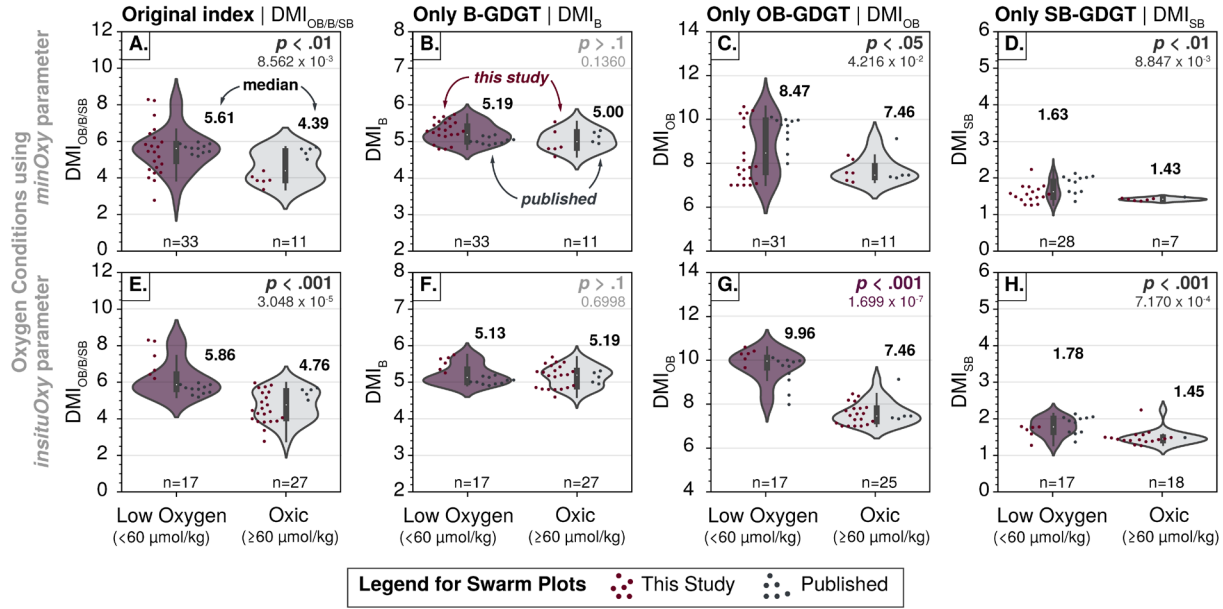


**Fig. 5. Ranges of methylation indices of core-top GDGT data at low oxygen and oxic conditions based on *minOxy* and *insituOxy* parameters.** GDGT data were classified into low oxygen (purple violins) and oxic (gray violins) conditions based on *minOxy* (top row) and *insituOxy* (BWO for core-top data; bottom row). Each column shows value ranges of different methylation indices discussed in this study, including the original methylation index  $MI_{OB/B/SB}$  (left) and three modified methylation indices based on only B-GDGT (middle left), OB-GDGT (middle right), and SB-GDGT (right) fractions. Violin plots show the distribution of methylation indices as a symmetric kernel density estimate (KDE) together with the inner box-and-whisker plot. White dots show the medians of each data cluster with the numerical annotations presented next to each violin plot. Swarm plots (dots) show the distribution of raw data points from this study (maroon) and published data (dark gray). Note: The annotated  $p$  values are from the non-parametric Mann-Whitney  $U$  test. Grey out annotated text indicates that the medians are *not significantly different* between low oxygen and oxic data clusters ( $p > .1$ ). Purple annotated text indicates the case with lowest  $p$  value across all comparisons. Actual  $p$  values up to fourth significance digit are shown below the reported significance level.

297 As B-GDGT fractions are known to have multiple sources, notably non-marine, we assess  
 298 if removing B-GDGT from the calculation will improve the separation between low oxygen and  
 299 oxic data clusters. The modified indices are expressed as follows:

$$DMI_{OB/B} = \frac{(\sum_{n=7}^{12} n * [X_{OB}] + \sum_{n=4}^6 n * [X_B])}{[\Sigma OB + \Sigma B]} \quad (2)$$

$$DMI_{B/SB} = \frac{(\sum_{n=4}^6 n * [X_B] + \sum_{n=0}^3 n * [X_{SB}])}{[\Sigma O + \Sigma SB]} \quad (3)$$

$$DMI_B = \frac{(\sum_{n=4}^6 n * [X_B])}{[\Sigma B]} \quad (4)$$

$$DMI_{SB} = \frac{(\sum_{n=0}^3 n * [X_{SB}])}{[\Sigma SB]} \quad (5)$$

$$DMI_{OB} = \frac{(\sum_{n=7}^{12} n * [X_{OB}])}{[\Sigma OB]} \quad (6)$$

300 The MWU test for these modified methylation indices shows that the medians of the  
301 methylation index based only on the B-GDGT series ( $DMI_B$ ) between the low oxygen and oxic  
302 data clusters are *not significantly different* ( $p > .1$ ; **Fig. 5B**). While the resulting  $p$  values for the  
303 methylation indices based only OB-GDGT ( $DMI_{OB}$ ) and SB-GDGT ( $DMI_{SB}$ ) series are below the  
304 standard significance level ( $p < .05$ ; **Figs. 5C and 5D**), suggesting that distributions of OB-GDGT  
305 and SB-GDGT are sensitive to *minOxy* and *insituOxy* levels. The greater difference in the medians  
306 between the low oxygen and oxic data clusters in the  $DMI_{OB}$ , i.e., the lower resulting  $p$  value,  
307 suggests that OB-GDGTs may be more sensitive to changes in oxygen conditions in the water  
308 column.

309 Although the discovery of OB-GDGT and SB-GDGT series and the establishment of the  
310  $DMI_{OB/B/SB}$  index were originally from studies that focus on regions with strong mid-depth OMZs  
311 or fully anoxic water columns (Liu et al., 2012, 2014; Xie et al., 2014), we expanded our  
312 assessment on the variation of methylation indices in response to changes in oxygen conditions at  
313 different locations in the water column using the calculated DO-derived parameters. Based on the  
314 nonparametric Spearman's rank correlation, the  $DMI_{OB/B/SB}$  show the overall negative correlation  
315 with oxygen conditions in the water column; higher  $DMI_{OB/B/SB}$  at lower oxygen conditions  
316 (Column 5 in **Fig. 6**). Across all seven DO-derived parameters, the *minOxy* parameter gives the  
317 highest Spearman's rank correlation coefficient (denoted as *rho* or  $\rho$ ) of -0.58 with the  $DMI_{OB/B/SB}$   
318 (Column 5 & Row 1 in **Fig. 6**). As suggested above by the MWU tests, the  $DMI_{OB}$  should show  
319 better responses to changes in oxygen conditions in the water column. However, correlation  
320 coefficients between *minOxy* and  $DMI_{OB}$  and  $DMI_{SB}$  indices exhibit similar ( $\rho = -0.59$ ) or stronger  
321 responses ( $\rho = -0.66$ ), respectively. Interestingly, the *insituOxy* gives a stronger Spearman's  $\rho$  with  
322 the  $DMI_{OB}$  (-0.78) than the *minOxy* parameter (C10 in **Fig. 6**). In fact, the Spearman's correlation  
323 between the *insituOxy* parameter and the  $DMI_{OB}$  shows the strongest correlation across the  
324 heatmap of the pairwise correlation (C10 & R2 in **Fig. 6**), hinting to us that changes in surface  
325 sediment OB-GDGT distributions might be largely controlled by oxygen conditions at the deep  
326 ocean instead of the intermediate depth. By repeating the MWU tests for the *insituOxy* case, we  
327 observe stronger differences in the medians between low oxygen and oxic data clusters, i.e., lower

**Core top (n = 44)**

Spearman's rank correlation coeff. ( $\rho$ )

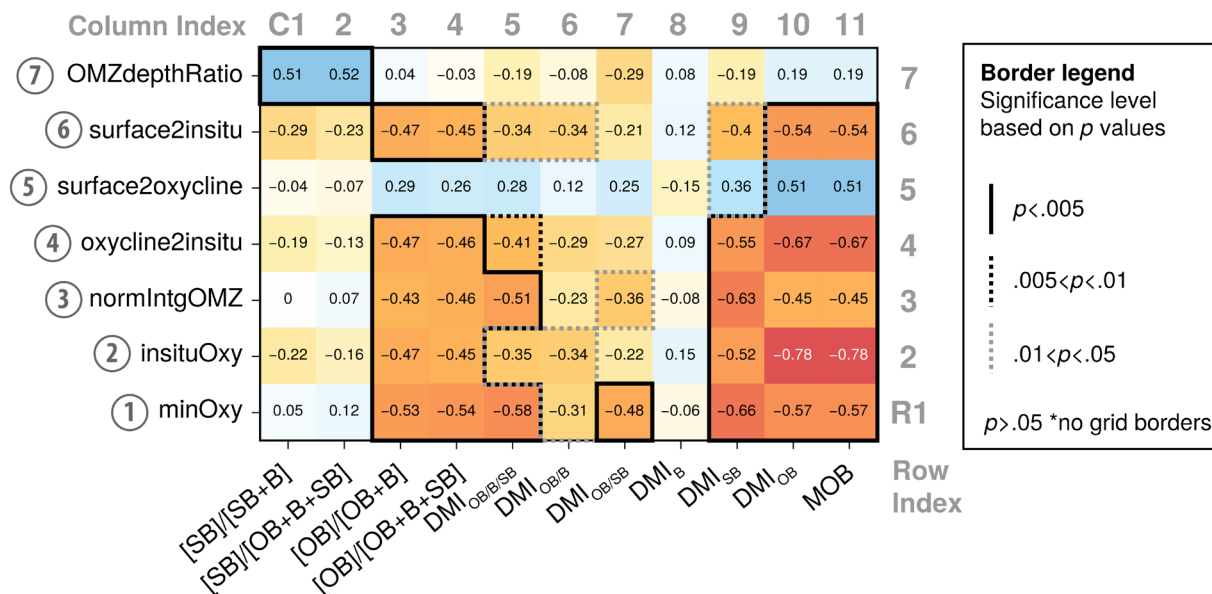


**Fig. 6. Pairwise correlation between brGDGT-derived indices and DO-derived parameters.** The heatmap shows Spearman's rank correlation coefficient ( $\rho$ ) between DO-derived parameters (rows) and GDGT-derived indices (columns) with the annotated numerical values rounded to the second decimal place. The "HotCold" color map emphasizes the direction of the trend between the two variables. The annotated grid borders indicate significance level based on  $p$  values:  $p < .005$  (solid black),  $.005 < p < .01$  (dashed black),  $.01 < p < .05$  (dashed gray), and  $p > .05$  (no border; *not statistically significance*). The position where each DO-derived parameter represent in the water column can be found in **Fig. 4**.

328  $p$  values, in all methylation indices except the DMI<sub>B</sub> (see the bottom row in **Fig. 5**). The largest  
 329 difference in the medians and the lowest  $p$  value observed from the DMI<sub>OB</sub> case (**Fig. 5G**), together  
 330 with the strongest Spearman's correlation (C10 & R2 in **Fig. 6**), all indicate that the OB-GDGTs  
 331 might be the GDGT fraction that is most sensitive to changes in oxygen conditions in the water  
 332 column. Across all analyses, it appears that changes in deep ocean oxygen conditions, i.e.,  
 333 specifically at the seawater-sediment interface in our study, exert stronger control over the  
 334 distribution of OB-GDGT and SB-GDGT in surface marine sediments than oxygen conditions of  
 335 the overlying water column.

### 3.2 Potential sources of OB-GDGT and SB-GDGT in marine sediments

337 Our statistical analyses over the extended data set of core-top brGDGTs suggest that the  
 338 likely sources of these lipids are heterotrophic bacteria thriving in the sediment-water interface,  
 339 rather than the mid-depth OMZs. This is in line with the observation from the water-column SPM  
 340 study in the EEP, showing that OB-GDGT and SB-GDGT are rapidly disappearing in the

341 oxygenated water masses below the mid-depth OMZs (Xie et al., 2014). However, the production  
342 of OB-GDGT in marine sediments below the seafloor could alter the original distribution of  
343 brGDGT in the surface sediments, challenging the idea of using these lipids as a geochemical  
344 proxy to reconstruct past changes in ocean oxygenation. Research by Zeng et al. (2023) suggests  
345 that OB-GDGTs are produced by anaerobic bacteria in subsurface sediments collected from the  
346 Mariana Trench, supported by the co-occurrence of a high abundance of bacterial 16S rRNA genes  
347 and an increase in the relative abundance of known anaerobic bacteria unique to abyssal marine  
348 sediments. Unfortunately, paired porewater chemistry profile critical for understanding the  
349 sediment column's redox condition of in the context of microbial ecology and lipid distribution  
350 changes were unavailable (Zeng et al., 2023). Additionally, studies on intact polar lipids, which  
351 are more closely related to living cells, suggest that they typically constitute a very small portion  
352 of GDGT found in the sediment column (typically <15%; cf. Lengger et al., 2014; Lipp and  
353 Hinrichs, 2009; Liu et al., 2011). Most sedimentary GDGTs fall into the core lipid fraction,  
354 representing the inactive pool long after cell lysis. Future work such as lipid analysis of bacterial  
355 cultures, is needed to confirm the extent to which these subsurface bacteria contribute to the  
356 sedimentary pool of OB-GDGTs. Intact polar lipids of OB-GDGTs can also help quantify the  
357 contribution of living bacteria to the total GDGT pool.

358 Another piece of evidence unfavorable for subsurface production as the primary source of  
359 these lipids comes from our analysis of brGDGT distributions from ancient marine sediments of  
360 ODP site 850, dated back 12 million years. If OB-GDGTs with higher degrees of methylation were  
361 primarily produced in subsurface anoxic sediments, we would expect higher  $DMI_{OB}$  values from  
362 the intervals where porewater chemistry clearly indicates redox condition changes (Shipboard  
363 Scientific Party, 1992). The presumed low oxygen conditions in downcore sediments start at  
364 approximately 110 meters below sea floor, where concentrations of porewater ammonia and  
365 methane gas increase with decreasing sulfate (Figs. 7D–F). The  $DMI_{OB}$  values within this  
366 presumed anoxic interval show a relatively low  $DMI_{OB}$  index, arguing against major *in situ* GDGT  
367 production by anaerobic bacteria in sediments. With the help of the global core-top data, we are  
368 able to infer bottom water oxygen levels through the temporal variation in the  $DMI_{OB}$  index.  
369 Mechanistically, these changes can be recorded by alterations in bacterial communities at the  
370 seawater-sediment interface or by physiological responses of cell membranes to different *in situ*  
371 oxygen levels by the same group of bacteria.

372 **3.3 Development of a proxy for deep ocean (de)oxygenation**

373 *3.3.1 The Methylation index of Overly Branched GDGTs (MOB)*

374 Although OB-GDGT and SB-GDGT series are present in most of core-top sediments in  
 375 the extended data set, SB-GDGTs are generally of very low abundance in downcore samples and  
 376 were often not reported in previous work (cf. Connock et al., 2022; Zeng et al., 2023). Due to their  
 377 low abundance, we did not report SB-GDGT fractions from our reanalyzed samples from ODP  
 378 850 (see Fig. 7A). Given that OB-GDGT fractions are observed in both modern and ancient marine  
 379 sediment archives, the  $DMI_{OB}$  index emerges as the most suitable index to be developed as a proxy  
 380 for tracking (de)oxygenation in past oceans. We normalized the  $DMI_{OB}$  index to the entire data set

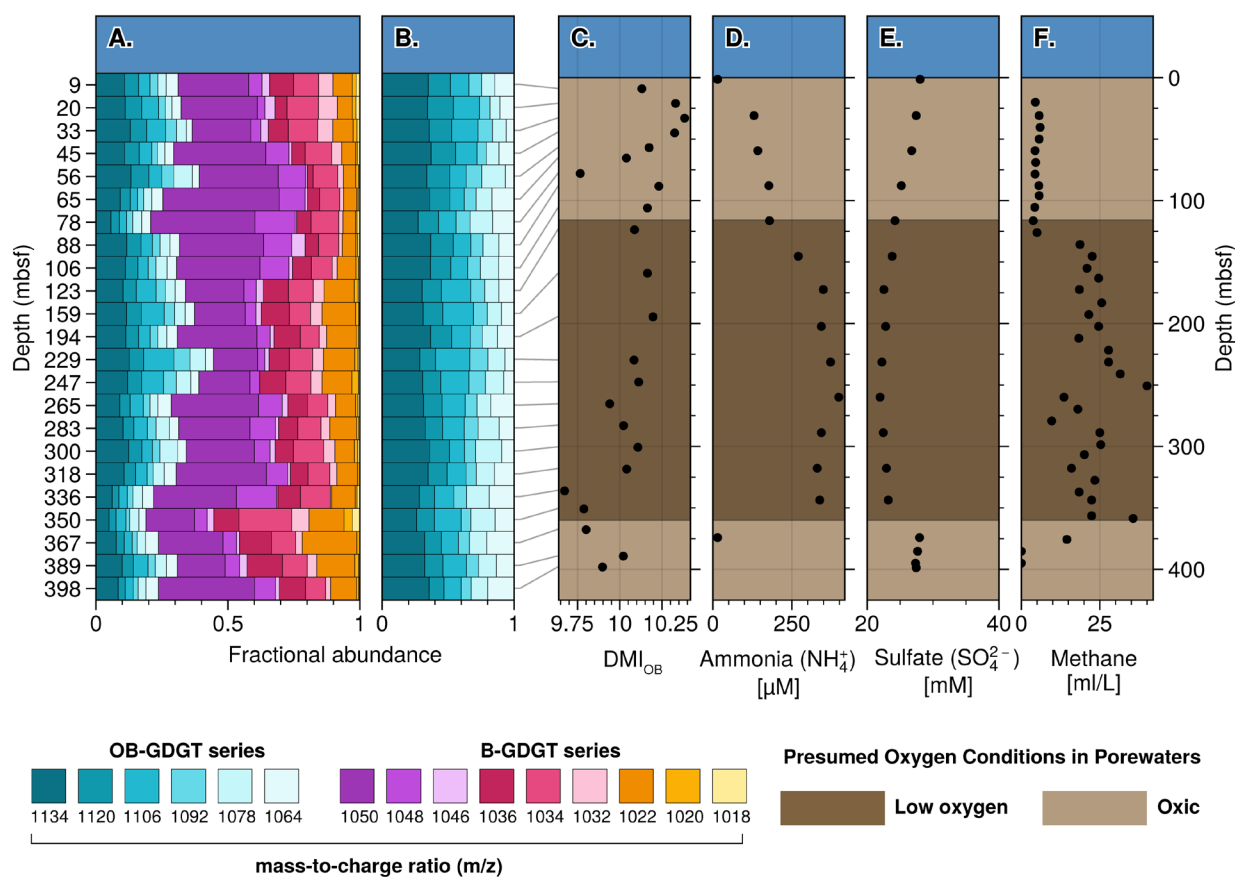


**Fig. 7. Downcore brGDGT distribution,  $DMI_{OB}$ , and porewater chemistry of sediments from Ocean Drilling Program site 850.** (A) Fractional abundances of OB-GDGT and B-GDGT series. (B) Fractional abundances of OB-GDGT series. (C) The modified methylation index uses only the OB-GDGT series ( $MI_{OB}$ ). The stored TLEs were analyzed samples used in Zhang et al. (2014) temperature reconstruction study. Concentrations of (D) porewater ammonia ( $NH_4^+$ ), (E) porewater sulfate ( $SO_4^{2-}$ ), and (F) methane gases in sediments collected during the ODP850 expedition (Shipboard Scientific Party, 1992). The dark brown layer indicates the presumed low oxygen conditions in sediments based on porewater chemistry. Note: Fractional abundances of brGDGTs were measured from the stored TLEs extracted from downcore sediments from the Ocean Drilling Program (ODP) site 850.

381 using the minimum-maximum scaling technique to scale the index value range to span from 0 to  
382 1 and named the **M**ethylation index of **O**verly **B**ranching GDGT as the **MOB** index:

$$MOB = \frac{(DMI_{OB})_{observed} - (DMI_{OB})_{min}}{(DMI_{OB})_{max} - (DMI_{OB})_{min}} \quad (7)$$

383 where  $(DMI_{OB})_{observed}$  is the methylation index of OB-GDGT derived from **equation (6)**. The  
384 theoretical minimum  $(DMI_{OB})_{min}$  and maximum  $(DMI_{OB})_{max}$  values of the  $DMI_{OB}$  index are 7 and  
385 12, respectively. Plugging these values into **equation (7)**, the MOB values can be calculated as  
386 follows:

$$MOB = \frac{(DMI_{OB})_{observed} - 7}{12 - 7} = \frac{(DMI_{OB})_{observed} - 7}{5} \quad (8)$$

387 The MOB index gives the same Spearman's correlation  $\rho$  as the  $DMI_{OB}$  with the strongest negative  
388 relationship against the *insituOxy* parameter (C11 & R2 in **Fig. 6**).

### 389 3.3.2 Bottom water oxygen calibrations based on the extended core-top data set.

390 Given the relatively small sample size ( $n = 42$ ) of the core-top data set, it is likely that the  
391 distributions of the MOB index and *insituOxy* are non-Gaussian. Plus, the value ranges of both  
392 parameters are strictly positive, including zeros  $[0, \infty)$ , suggesting that the ordinary least square  
393 (OLS) might not be the most suitable choice of regression model as it assumes that the MOB and  
394 *insituOxy* can go to negative values. Utilizing the *Tweedie Regressor* from the *scikit-learn* Python  
395 library, we found that the Poisson-like regression (power = 1.0) provides the highest deviance  
396 score ( $D^2 = 0.66$ ;  $p = 0.06$ ; see **Figs. 8A** and **8C**). The Poisson-like regression is the Generalized  
397 Linear Model (GLM) with the natural log link function and can be expressed in the following  
398 form:

$$Y = e^{\alpha + \beta \cdot X} + \epsilon \quad (9)$$

399 where the target  $Y$  value is the exponential of a linear model with intercept ( $\alpha$ ), slope ( $\beta$ ), and  
400 random noise ( $\epsilon$ ). The quality of each Poisson-like regression is quantified by the percentage of  
401 deviance explained ( $D^2$ ) of the GLM; the score that is equivalent to the coefficient of determination

402  $r^2$  in the OLS regression.

403 Although we have expanded the core-top collection with samples from sites represented a  
 404 wider range of oxygen conditions in water column, the regression curves could still be heavily  
 405 biased towards this anoxic/euxinic basin as data from the Black Sea ( $n = 12$ ) represented  $\sim 29\%$  of  
 406 the entire core-top collection ( $n = 42$ ). We repeated the same set of regressions on the subset of  
 407 core top data excluding the Black Sea data to provide alternative calibrations that may be more  
 408 suitable for open-ocean settings. Similarly, the Poisson-like regression also gives the highest  
 409 deviance score the *insituOxy* and MOB parameters ( $D^2 = 0.67$ ;  $p = 0.09$ ; see **Figs. 8B** and **8D**).  
 410 However, the y-intercept of the latter case is higher than the regression curve of the full core-top  
 411 dataset. To fully capture the possible range of estimated  $Y$  values at any given  $X$ , we computed the  
 412 95% confidence interval of the Poisson-like regression curves by randomly sampling  $\alpha$  and  $\beta$

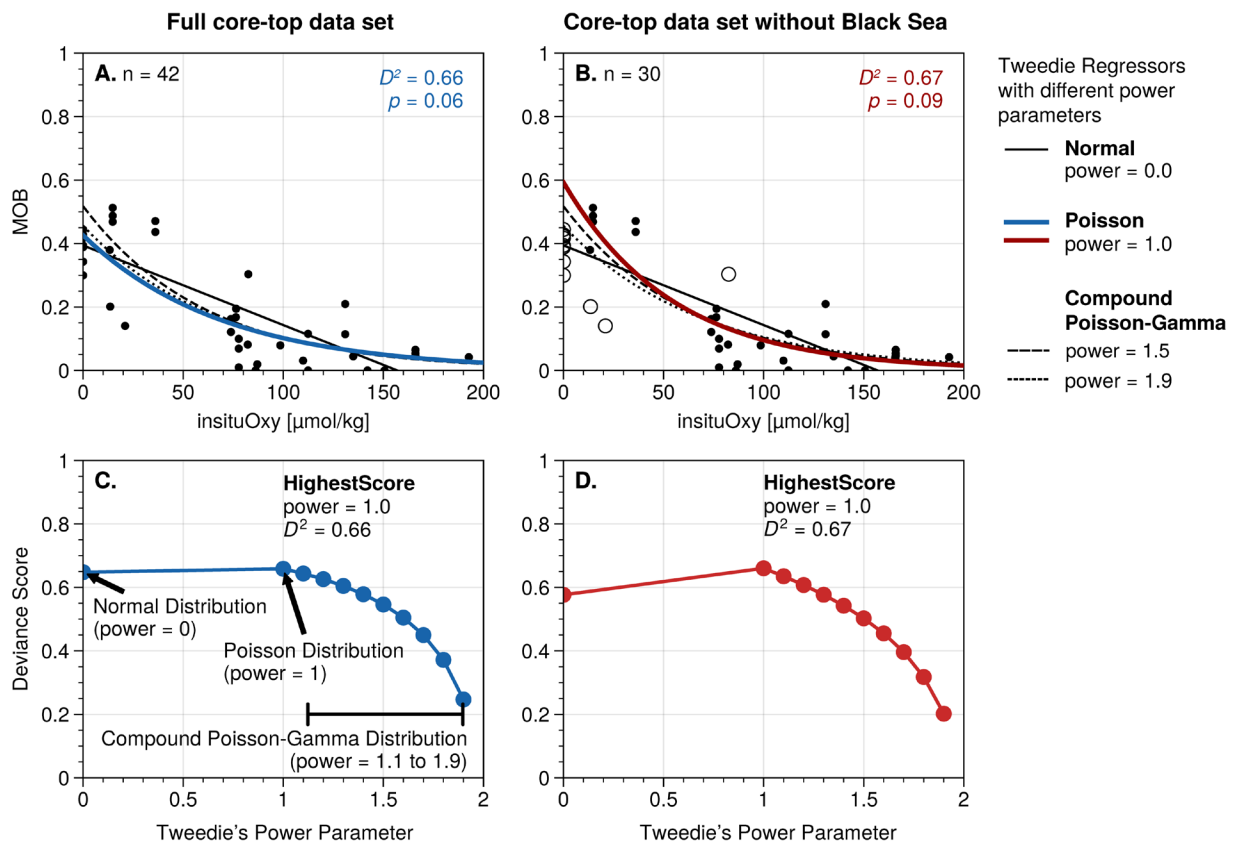


**Fig. 8. Different calibration curves based on the extended core-top GDGT data set.** Several choices of calibration curves are displayed over MOB-insituOxy scatter plots based on (A) the full core-top and (B) the core-top data set without the Black Sea samples. Calibration curves result from generalized linear models (GLM) with different Tweedie's power parameters. At different power parameters, GLM predicts the MOB values (fitted MOB) by assuming that fitted  $Y$  values belong to a distribution in the exponential dispersion model (EDM), including the Normal (power = 0.0), the Poisson (power = 1.0), and the Compound Poisson-Gamma (power = 1.1-1.9) distributions. (Bottom) Deviance scores for each GLM regression result at different Tweedie's power parameters for (C) the full core-top data set and (D) the subset of GDGT collection without the Black Sea.

413 parameters using the Markov Chain Monte Carlo (MCMC) technique (**Figs. 9A** and **9B**). Although  
 414 the deviance score is only slightly improved without Black Sea data in the core-top data set, the  
 415 Poisson-like regression based on this subset is preferred for the *insituOxy*-MOB core-top  
 416 calibration as the resulting MOB residuals show no relationship with the fitted MOB values (**Fig.**  
 417 **9G**). The fitted MOB values based on the full data set show a stronger regression bias, i.e. higher  
 418  $r^2$  in the residual plot (**Fig. 9F**). **Table 2** shows slopes and intercepts of both regression scenarios.

### 419 3.4 Application of MOB: EEP deoxygenation over the past 12 million years

420 As previously discussed, we view that the down-core variation in the MOB index as likely  
 421 reflecting bacterial community at the seawater-sediment interface in response to different levels of

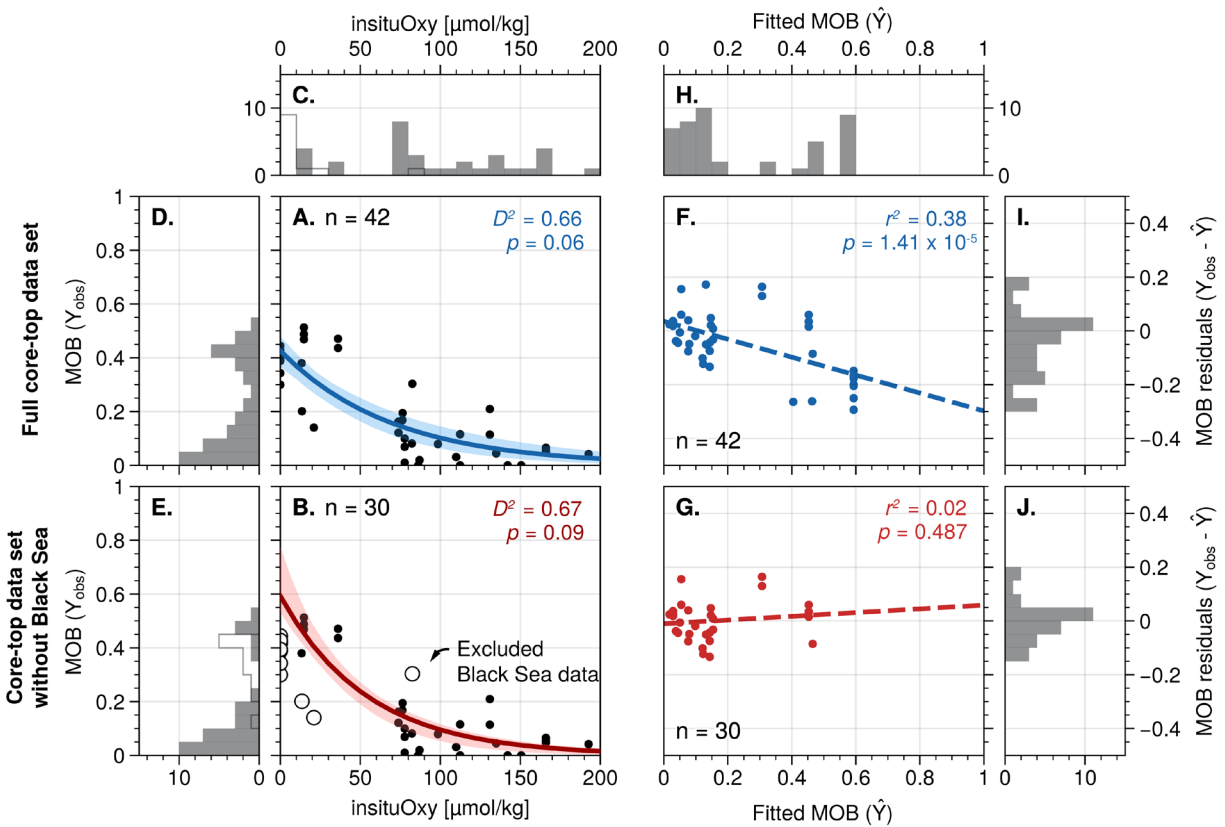


**Fig. 9. Poisson-like regressions between *insituOxy* and MOB index with residual plots based on the full core-top data set (top) and the subset without Black Sea data (bottom).** (A) The Poisson-like regression curve of the full core-top data set with the annotated deviance score ( $D^2$ ) and the  $p$  value. The shaded area represents the 95% confidence interval of the Poisson-like regression line using the Markov Chain Monte Carlo technique to capture the full range of regression slopes and intercepts. (B) The scatter plot of the residuals between the observed and fitted MOB values (observed MOB - fitted MOB) with associated  $r^2$  and  $p$  values. (F) and (G) are the same regression analysis as (A) and (B) but for the subset of core-top collection with the Black Sea data. (C-E and H-J) Histograms show data distributions of  $X$  and  $Y$  variables of each scatter plot.

**Table 2.** Slopes and intercepts for Poisson-like regression curves discussed in main text.

Case No.	Equation	Intercept ( $\alpha$ )	Slope ( $\beta$ )	$D^2$	$p$ value	Ref. Fig.
<b>Poisson-like regression</b>						
$MOB = \exp(\alpha + \beta \cdot insituOxy) + \varepsilon$ <b>Equation (9)</b>						
(1)	Full core-top data set	-0.8535	-0.01431	0.66	0.06	Fig. 8A
(2)	Core-top data set without Black Sea	-0.5223	-0.01827	0.67	0.09	Fig. 8B

422 bottom water  $O_2$  concentrations, referred to as *insituOxy* parameter in this study, over geologic  
423 history. Using the Poisson-like regression parameters for the open ocean case (without Black Sea  
424 data; **Regression Case 2** in **Table 2**), the estimated *insituOxy* concentrations based on the MOB  
425 index show that the bottom water masses at ODP Site 850 underwent low DO conditions for the  
426 entire 12-myr record. Reconstructed *insituOxy* estimates gradually decreased from approximately  
427  $20 \mu\text{mol}\cdot\text{kg}^{-1}$  during the late Miocene to approximately  $10 \mu\text{mol}\cdot\text{kg}^{-1}$  during the Plio-Pliocene  
428 epochs with two spikes of increasing *insituOxy* observed around 10 and 4 million years ago (**Fig.**  
429 **10A**). Although there are no equivalent independent proxy records to confirm the reconstructed  
430 *insituOxy* concentrations based on the MOB index, some indirect evidence suggests that deep  
431 water in EEP experienced low  $O_2$  conditions during cooling episodes. For example, several  
432 reconstructions of bottom water  $O_2$  levels based on redox-sensitive authigenic uranium derived  
433 from marine sediments spanning the last 180,000 years show the lowest values during glacial  
434 periods, suggesting an increased extent of respired carbon in the deep ocean (cf. [Marcantonio et](#)  
435 [al., 2020](#)). In addition, estimated changes in bottom water  $O_2$  concentrations based on the output  
436 of a geochemical box model CYCLOPS in the deep Pacific during the Last Glacial Maximum  
437 relative to the Holocene can be up to approximately  $80\text{--}100 \mu\text{mol}\cdot\text{kg}^{-1}$  (see a thorough discussion  
438 in [Studer et al., 2021](#)), reflecting low  $O_2$  concentrations in the deep Pacific.

439 Variation in oxygen supply to deep ocean waters could also be attributed to changes in  
440 climate and ocean circulation. The cooling climate during the Neogene ([Herbert et al., 2016](#);  
441 [Zachos et al., 2001](#)), the development of modern-like Antarctic Circumpolar Current since the late  
442 Miocene ([Evangelinos et al., 2024](#)), and the intensification of Pacific Deep Water circulation since  
443 the early Pliocene ([Yin et al., 2022](#)) all could have caused an increase in deep-water DO  
444 concentrations due to (i) greater gas solubility in colder seawaters and (ii) stronger export of  
445 oxygen-rich deep water masses from high-latitude formation sites. Yet, our interpreted low DO

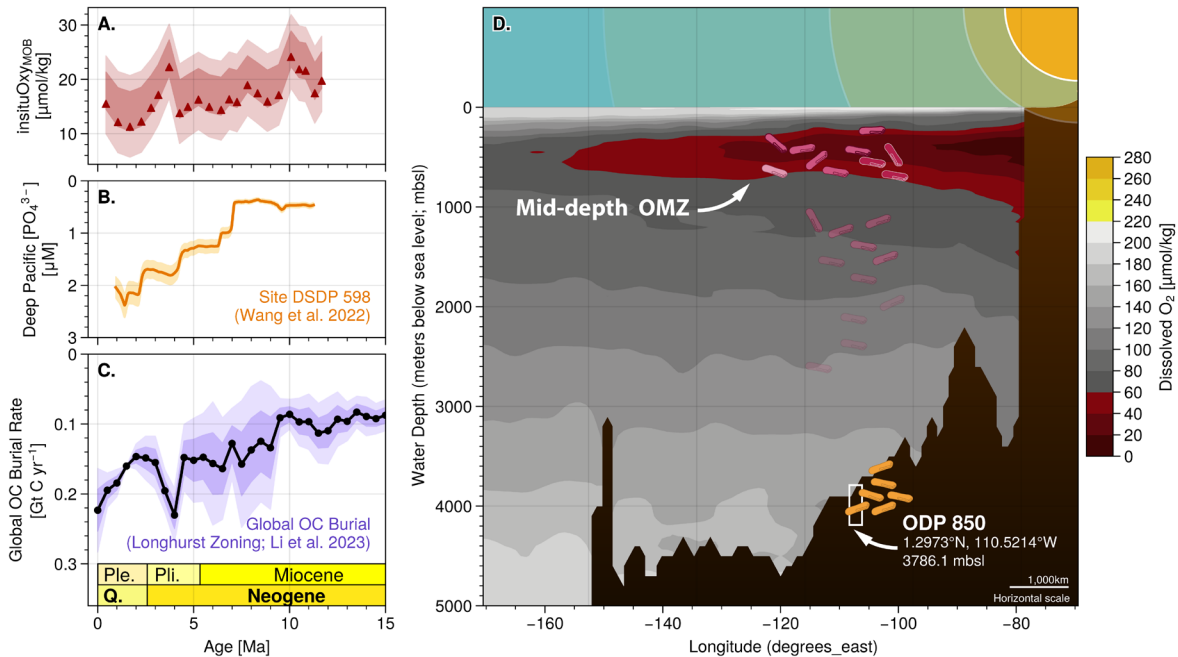


**Fig. 10. 12-my records of the MOB index in the Eastern Pacific Ocean.** (A) Reconstructed *insituOxy* based on Poisson-like (log-linear) calibration. Red triangles represent the estimated *insituOxy* based on regression parameters resulting from the data set without the Black Sea data (Case 2 in Table 2). Shaded bands show the corresponding confidence intervals of 68% ( $\pm 1\sigma$ ) and 95% ( $\pm 2\sigma$ ), estimated using an MCMC approach. (B) Deep Pacific phosphate concentrations [ $\text{PO}_4^{3-}$ ] reconstructed from the nearby ocean drilling site DSDP 598 in the EEP region. Increases in deep-water [ $\text{PO}_4^{3-}$ ] over the past 12 myr reflect the declining level of deep ocean DO, as previously discussed by Wang et al., (2022). (D) Graphical sketch shows the proposed mechanism how oxygen conditions in deep Pacific changes over time at ODP site 850.

446 conditions in the deep EEP based on the MOB index parallels with the observed increase in deep  
 447 Pacific water phosphate levels (see **Figs. 9B** and **9C**; Wang et al., 2022) and the overall increase  
 448 in global organic carbon burial rate over the last 15 Ma (Li et al., 2023), suggesting to us that  
 449 enhanced oxygen supply was outcompeted by higher oxygen demand attributed to increased export  
 450 productivity. It remains unclear whether declining oxygen levels drive enhanced export  
 451 productivity and nutrient enrichment, or if they are merely a response to increased organic matter  
 452 export and subsequent degradation. Nonetheless, the secular trend of increasing bottom water  
 453 nutrient levels, declining oxygen concentrations, and enhanced organic carbon burial in sediments  
 454 presents a coherent narrative of ocean biogeochemical changes since the middle Miocene in the  
 455 EEP region, carrying important implications for long-term climatic and oceanic changes.

456 Despite incorporating the shallowest sample from ODP Site 850 into the core-top  
 457 collection, it is still possible that the absolute values of reconstructed *insituOxy* concentrations  
 458 based on our current calibration are still be biased towards lower DO levels given the limited extent

459 of represented sites in the current data set. However, this first iteration of MOB proxy development  
460 shows that the variation in methylation index of OB-GDGT can track the overall declining trend  
461 of deep ocean DO concentrations. Future studies with additional GDGT measurements from a  
462 wider range of core-top sites can be easily incorporated into the calibration framework using the  
463 Python codes (see Supplementary Information) and would improve the accuracy of the absolute  
464 *insituOxy* estimates based on the MOB index.

### 465 **3.5 Potential avenues for future works**

466 Similar to other well-established GDGT-based proxies like MBT/CBT and TEX<sub>86</sub>, which  
467 have provided major insights into Earth's past environments despite initially limited information  
468 on the source organisms, the MOB proxy could offer unique insights into past oceanic redox  
469 conditions, with profound implications for understanding the co-evolution of life and global  
470 biogeochemical cycles. While our interpretation relies on certain assumptions, the empirical  
471 relationship between MOB values and bottom water oxygen levels observed in the core-top study  
472 is a promising beginning. Future work is needed to validate and refine this proxy; for example,  
473 identifying source organisms of these lipid compounds. Furthermore, confirming the resistance of  
474 OB-GDGTs to early diagenesis or understanding any potential preferential degradation patterns  
475 would strengthen the robustness of this proxy.

## 476 **4 Conclusions**

477 Since its first discovery from core-top sediments in the EEP region (Liu et al., 2012), OB-  
478 GDGTs have demonstrated great potential to be a geochemical proxy for past marine  
479 (de)oxygenation. Building upon the original methylation index of brGDGTs (DMI<sub>OB/B/SB</sub>), we  
480 explored relationships between various combinations of brGDGT ratios/indices and environmental  
481 variables related to DO in ocean water columns. We found that the modified methylation index  
482 using only OB-GDGT (DMI<sub>OB</sub>) in the core top data set gives the strongest response to *insituOxy*  
483 concentrations. Applying the proposed MOB index to the paleo GDGT record spanning the last  
484 12 myr from the EEP region suggests to us that the index can track progressive deoxygenation in  
485 the deep Pacific parallel to the elevated nutrient level of the Pacific deep water (Wang et al., 2022)  
486 and enhanced burial of organic carbon globally (Li et al., 2023). Regression analyses performed  
487 in this work can easily accommodate new core-top data, when available, to improve the accuracy

488 of the prediction model for bottom water oxygen concentrations. Our findings demonstrate the  
489 MOB index's potential for tracking relative changes in deep-ocean (de)oxygenation through time,  
490 highlighting its promising application as a proxy for past oceanic redox conditions intrinsically  
491 linked to global biogeochemical cycles and climate history.

492 **Data Availability Statement.**

493 **GDGT data.** Published GDGT fractional abundance data used for in the study are directly  
494 retrieved from [Liu et al. \(2014\)](#) and [Zeng et al. \(2023\)](#). The curated data sets of these data together  
495 with new GDGT data determined by this study are available as supplementary materials in this  
496 article and are deposited online at Figshare (public link will be provided upon acceptance) and  
497 GitHub repositories (to be provided at the proofing stage, if accepted).

498 **Python codes.** Jupyter Notebooks (\*.ipynb) containing Python codes that were used for data  
499 preparation, statistical analyses, and data visualization are also deposited at Figshare repositories  
500 (to be provided at the proofing stage, if accepted) and available at  
501 [github.com/PaleoLipidRR/brGDGT-oxy-proxy/](https://github.com/PaleoLipidRR/brGDGT-oxy-proxy/) (to be published at the proofing stage, if accepted)  
502 or upon request from the corresponding author

503 **CRedit authorship contribution statement.**

504 **Ronnakrit Rattanasriampaipong:** Writing – original draft, Writing – review & editing,  
505 Visualization, Formal analysis, Conceptualization, Investigation, Data Curation, Methodology.

506 **Yi Ge Zhang:** Conceptualization, Writing – review & editing, Methodology, Coordination and  
507 oversees the project.

508 **Olawale Alo:** Methodology – GDGT determination, Writing – review & editing,

509 **Xiao-Lei Liu:** Methodology – GDGT determination, Writing – review & editing,

510 **Yang Zhang:** Methodology – GDGT determination

511 **Bumsoo Kim:** Methodology – Sample preparation, Writing – review & editing

512 **Franco Marcantonio:** Writing – review & editing, Resources – obtain sediment materials

513 **Franck Bassinot:** Resources – obtain sediment materials

514 **Tiegang Li:** Resources – obtain sediment materials

515

516 **Acknowledgement.**

517 We thank the captains and scientific/operational crews of all research cruises from which samples  
518 used in this study were obtained, including R/V *Melville* (2010 campaign), R/V *Marion Dufresne*  
519 (*OSIRIS 3* campaign), R/V *Baruna Jaya I* (BARAT campaign), and R/V *Ke Xue Yi Hao* (2012

520 campaign). We thank Ethan Grossman, Jason Sylvan, and Robert Korty for their thoughtful  
521 comments and discussion. Partial financial support for this study was provided by the Texas A&M  
522 University Dissertation Fellowship and NOAA Climate & Global Change Postdoctoral Fellowship  
523 administered by UCAR's Cooperative Programs for the Advancement of Earth System Science  
524 (CPAESS) under the NOAA Science Collaboration Program award (NA21OAR4310383) to R.R.,  
525 Guangzhou Institute of Geochemistry and Chinese Academy of Sciences Start-up support for  
526 Y.G.Z, Texas Sea Grant Grants-In-Aid of Graduate Research Program (NA18OAR4170088) to  
527 B.K.

528

529 **Declaration of competing interest.** The authors declare that they have no known competing  
530 financial interests or personal relationships that could have appeared to influence the work reported  
531 in this paper.

532

533

534 **References**

- 535 Arévalo-Martínez, D.L., Kock, A., Löscher, C.R., Schmitz, R.A., Bange, H.W., 2015. Massive  
536 nitrous oxide emissions from the tropical South Pacific Ocean. *Nat. Geosci.* 8, 530–533.  
537 <https://doi.org/10.1038/ngeo2469>
- 538 Auderset, A., Martínez-García, A., Tiedemann, R., Hasenfratz, A.P., Eglinton, T.I., Schiebel, R.,  
539 Sigman, D.M., Haug, G.H., 2019. Gulf Stream intensification after the early Pliocene  
540 shoaling of the Central American Seaway. *Earth Planet. Sci. Lett.* 520, 268–278.  
541 <https://doi.org/10.1016/j.epsl.2019.05.022>
- 542 Barras, C., Mouret, A., Nardelli, M.P., Metzger, E., Petersen, J., La, C., Filipsson, H.L., Jorissen,  
543 F., 2018. Experimental calibration of manganese incorporation in foraminiferal calcite.  
544 *Geochim. Cosmochim. Acta* 237, 49–64. <https://doi.org/10.1016/j.gca.2018.06.009>
- 545 Bennett, W.W., Canfield, D.E., 2020. Redox-sensitive trace metals as paleoredox proxies: A  
546 review and analysis of data from modern sediments. *Earth-Sci. Rev.* 204, 103175.  
547 <https://doi.org/10.1016/j.earscirev.2020.103175>
- 548 Breitburg, D., Levin, L.A., Oschlies, A., Grégoire, M., Chavez, F.P., Conley, D.J., Garçon, V.,  
549 Gilbert, D., Gutiérrez, D., Isensee, K., Jacinto, G.S., Limburg, K.E., Montes, I., Naqvi,  
550 S.W.A., Pitcher, G.C., Rabalais, N.N., Roman, M.R., Rose, K.A., Seibel, B.A.,  
551 Telszewski, M., Yasuhara, M., Zhang, J., 2018. Declining oxygen in the global ocean and  
552 coastal waters. *Science* 359, eaam7240. <https://doi.org/10.1126/science.aam7240>
- 553 Buckles, L.K., Weijers, J.W.H., Verschuren, D., Sinninghe Damsté, J.S., 2014. Sources of core  
554 and intact branched tetraether membrane lipids in the lacustrine environment: Anatomy  
555 of Lake Challa and its catchment, equatorial East Africa. *Geochim. Cosmochim. Acta*  
556 140, 106–126. <https://doi.org/10.1016/j.gca.2014.04.042>
- 557 Busecke, J.J.M., Resplandy, L., Ditkovsky, S.J., John, J.G., 2022. Diverging Fates of the Pacific  
558 Ocean Oxygen Minimum Zone and Its Core in a Warming World. *AGU Advances* 3,  
559 e2021AV000470. <https://doi.org/10.1029/2021AV000470>
- 560 Cabré, A., Marinov, I., Bernardello, R., Bianchi, D., 2015. Oxygen minimum zones in the  
561 tropical Pacific across CMIP5 models: mean state differences and climate change trends.  
562 *Biogeosciences* 12, 5429–5454. <https://doi.org/10.5194/bg-12-5429-2015>
- 563 Chen, Y., Zheng, F., Yang, H., Yang, W., Wu, R., Liu, X., Liang, H., Chen, H., Pei, H., Zhang,  
564 C., Pancost, R.D., Zeng, Z., 2022. The production of diverse brGDGTs by an  
565 Acidobacterium providing a physiological basis for paleoclimate proxies. *Geochim.*  
566 *Cosmochim. Acta* 337, 155–165. <https://doi.org/10.1016/j.gca.2022.08.033>
- 567 Connock, G.T., Owens, J.D., Liu, X.-L., 2022. Biotic induction and microbial ecological  
568 dynamics of Oceanic Anoxic Event 2. *Communications Earth & Environment* 3, 136.  
569 <https://doi.org/10.1038/s43247-022-00466-x>
- 570 Cooley, S., Schoeman, D., Bopp, L., Boyd, P., Donner, S., Ito, S.-I., Kiessling, W., Martinetto,  
571 P., Ojea, E., Racault, M.-F., 2022. Oceans and coastal ecosystems and their services, in:  
572 IPCC AR6 WGII. Cambridge University Press.
- 573 De Jonge, C., Stadnitskaia, A., Hopmans, E.C., Cherkashov, G., Fedotov, A., Sinninghe Damsté,  
574 J.S., 2014. In situ produced branched glycerol dialkyl glycerol tetraethers in suspended  
575 particulate matter from the Yenisei River, Eastern Siberia. *Geochim. Cosmochim. Acta*  
576 125, 476–491. <https://doi.org/10.1016/j.gca.2013.10.031>
- 577 Ding, S., Kohlhepp, B., Trumbore, S., Küsel, K., Totsche, K.-U., Pohnert, G., Gleixner, G.,  
578 Schwab, V.F., 2018. In situ production of core and intact bacterial and archaeal tetraether  
579 lipids in groundwater. *Org. Geochem.* 126, 1–12.

- 580 <https://doi.org/10.1016/j.orggeochem.2018.10.005>
- 581 Evangelinos, D., Etourneau, J., van de Flierdt, T., Crosta, X., Jeandel, C., Flores, J.-A., Harwood,  
582 D.M., Valero, L., Ducassou, E., Sauermilch, I., Klocker, A., Cacho, I., Pena, L.D.,  
583 Kreissig, K., Benoit, M., Belhadj, M., Paredes, E., Garcia-Solsona, E., López-Quirós, A.,  
584 Salabarnada, A., Escutia, C., 2024. Late Miocene onset of the modern Antarctic  
585 Circumpolar Current. *Nat. Geosci.* 17, 165–170. [https://doi.org/10.1038/s41561-023-](https://doi.org/10.1038/s41561-023-01356-3)  
586 [01356-3](https://doi.org/10.1038/s41561-023-01356-3)
- 587 Garcia, H.E., Weathers, K.W., Paver, C.R., Smolyar, I., Boyer, T.P., Locarnini, M.M., Zweng,  
588 M.M., Mishonov, A.V., Baranova, O.K., Seidov, D., 2019. *World Ocean Atlas 2018,*  
589 *Volume 3: Dissolved Oxygen, Apparent Oxygen Utilization, and Dissolved Oxygen*  
590 *Saturation.*
- 591 Glock, N., Eisenhauer, A., Milker, Y., Liebetrau, V., Schönfeld, J., Mallon, J., Sommer, S.,  
592 Hensen, C., 2011. ENVIRONMENTAL INFLUENCES ON THE PORE DENSITY OF  
593 BOLIVINA SPISSA (CUSHMAN). *J. Foraminiferal Res.* 41, 22–32.  
594 <https://doi.org/10.2113/gsjfr.41.1.22>
- 595 Glock, N., Liebetrau, V., Eisenhauer, A., 2014. I/Ca ratios in benthic foraminifera from the  
596 Peruvian oxygen minimum zone: analytical methodology and evaluation as proxy for  
597 redox conditions. *Biogeosci. Discuss.* 11, 11635–11670. [https://doi.org/10.5194/bgd-11-](https://doi.org/10.5194/bgd-11-11635-2014)  
598 [11635-2014](https://doi.org/10.5194/bgd-11-11635-2014)
- 599 Guichard, F., Hardjawidjaksana, K., 1994. BARAT 94 cruise, R/V *Baruna Jaya I.*
- 600 Halamka, T.A., McFarlin, J.M., Younkin, A.D., Depoy, J., Dildar, N., Kopf, S.H., 2021. Oxygen  
601 limitation can trigger the production of branched GDGTs in culture. *Geochemical*  
602 *Perspectives Letters* 19, 36–39. <https://doi.org/10.7185/geochemlet.2132>
- 603 Halamka, T.A., Raberg, J.H., McFarlin, J.M., Younkin, A.D., Mulligan, C., Liu, X.-L., Kopf,  
604 S.H., 2023. Production of diverse brGDGTs by *Acidobacterium Solibacter usitatus* in  
605 response to temperature, pH, and O<sub>2</sub> provides a culturing perspective on brGDGT  
606 proxies and biosynthesis. *Geobiology* 21, 102–118. <https://doi.org/10.1111/gbi.12525>
- 607 Herbert, T.D., Lawrence, K.T., Tzanova, A., Peterson, L.C., Caballero-Gill, R., Kelly, C.S.,  
608 2016. Late Miocene global cooling and the rise of modern ecosystems. *Nat. Geosci.* 9,  
609 843.  
610 <https://doi.org/10.1038/ngeo2813>[https://www.nature.com/articles/ngeo2813#supplementa](https://www.nature.com/articles/ngeo2813#supplementary-information)  
611 [ry-information](https://www.nature.com/articles/ngeo2813#supplementary-information)
- 612 Hess, A.V., Auderset, A., Rosenthal, Y., Miller, K.G., Zhou, X., Sigman, D.M., Martínez-García,  
613 A., 2023. A well-oxygenated eastern tropical Pacific during the warm Miocene. *Nature*  
614 619, 521–525. <https://doi.org/10.1038/s41586-023-06104-6>
- 615 Hopmans, E.C., Weijers, J.W.H., Schefuß, E., Herfort, L., Sinninghe Damsté, J.S., Schouten, S.,  
616 2004. A novel proxy for terrestrial organic matter in sediments based on branched and  
617 isoprenoid tetraether lipids. *Earth Planet. Sci. Lett.* 224, 107–116.  
618 <https://doi.org/10.1016/j.epsl.2004.05.012>
- 619 Hoyer, S., Hamman, J., 2017. xarray: ND labeled arrays and datasets in Python. *Journal of Open*  
620 *Research Software* 5.
- 621 Huguet, C., Schimmelmann, A., Thunell, R., Lourens, L.J., Sinninghe Damsté, J.S., Schouten, S.,  
622 2007. A study of the TEX86 paleothermometer in the water column and sediments of the  
623 Santa Barbara Basin, California. *Paleoceanography* 22.  
624 <https://doi.org/10.1029/2006pa001310>
- 625 Jean-Claude, D., 1977. OSIRIS 3 - MD 13 cruise, R/V *Marion Dufresne.*

- 626 Jenny, J.-P., Francus, P., Normandeau, A., Lapointe, F., Perga, M.-E., Ojala, A., Schimmelmann,  
627 A., Zolitschka, B., 2016. Global spread of hypoxia in freshwater ecosystems during the  
628 last three centuries is caused by rising local human pressure. *Glob. Chang. Biol.* 22,  
629 1481–1489. <https://doi.org/10.1111/gcb.13193>
- 630 Ji, Q., Buitenhuis, E., Suntharalingam, P., Sarmiento, J.L., Ward, B.B., 2018. Global nitrous  
631 oxide production determined by oxygen sensitivity of nitrification and denitrification.  
632 *Global Biogeochem. Cycles* 32, 1790–1802. <https://doi.org/10.1029/2018gb005887>
- 633 Lengger, S.K., Hopmans, E.C., Sinninghe Damsté, J.S., Schouten, S., 2014. Fossilization and  
634 degradation of archaeal intact polar tetraether lipids in deeply buried marine sediments  
635 (Peru Margin). *Geobiology* 12, 212–220. <https://doi.org/10.1111/gbi.12081>
- 636 Li, H., Lü, X., Tao, C., Han, T., Hu, P., Zhang, G., Yu, Z., Dong, C., Shao, Z., 2018. Distribution  
637 of tetraether lipids in sulfide chimneys at the Deyin hydrothermal field, southern Mid-  
638 Atlantic Ridge: Implication to chimney growing stage. *Sci. Rep.* 8, 8060.  
639 <https://doi.org/10.1038/s41598-018-26166-1>
- 640 Li, Z., Zhang, Y.G., Torres, M., Mills, B.J.W., 2023. Neogene burial of organic carbon in the  
641 global ocean. *Nature* 613, 90–95. <https://doi.org/10.1038/s41586-022-05413-6>
- 642 Lipp, J.S., Hinrichs, K.-U., 2009. Structural diversity and fate of intact polar lipids in marine  
643 sediments. *Geochim. Cosmochim. Acta* 73, 6816–6833.  
644 <https://doi.org/10.1016/j.gca.2009.08.003>
- 645 Liu, X., Lipp, J.S., Hinrichs, K.-U., 2011. Distribution of intact and core GDGTs in marine  
646 sediments. *Org. Geochem.* 42, 368–375.  
647 <https://doi.org/10.1016/j.orggeochem.2011.02.003>
- 648 Liu, X.-L., Summons, R.E., Hinrichs, K.-U., 2012. Extending the known range of glycerol ether  
649 lipids in the environment: structural assignments based on tandem mass spectral  
650 fragmentation patterns. *Rapid Commun. Mass Spectrom.* 26, 2295–2302.  
651 <https://doi.org/10.1002/rcm.6355>
- 652 Liu, X.-L., Zhu, C., Wakeham, S.G., Hinrichs, K.-U., 2014. In situ production of branched  
653 glycerol dialkyl glycerol tetraethers in anoxic marine water columns. *Mar. Chem.* 166, 1–  
654 8. <https://doi.org/10.1016/j.marchem.2014.08.008>
- 655 Lu, W., Rickaby, R.E.M., Hoogakker, B.A.A., Rathburn, A.E., Burkett, A.M., Dickson, A.J.,  
656 Martínez-Méndez, G., Hillenbrand, C.-D., Zhou, X., Thomas, E., Lu, Z., 2020. I/Ca in  
657 epifaunal benthic foraminifera: A semi-quantitative proxy for bottom water oxygen in a  
658 multi-proxy compilation for glacial ocean deoxygenation. *Earth Planet. Sci. Lett.* 533,  
659 116055. <https://doi.org/10.1016/j.epsl.2019.116055>
- 660 Marcantonio, F., Hostak, R., Hertzberg, J.E., Schmidt, M.W., 2020. Deep Equatorial Pacific  
661 Ocean Oxygenation and Atmospheric CO<sub>2</sub> Over The Last Ice Age. *Sci. Rep.* 10, 6606.  
662 <https://doi.org/10.1038/s41598-020-63628-x>
- 663 Marcantonio, F., Lyle, M., Ibrahim, R., 2014. Particle sorting during sediment redistribution  
664 processes and the effect on <sup>230</sup>Th-normalized mass accumulation rates. *Geophys. Res.*  
665 *Lett.* 41, 5547–5554. <https://doi.org/10.1002/2014GL060477>
- 666 Martínez-Sosa, P., Tierney, J.E., Stefanescu, I.C., Dearing Crampton-Flood, E., Shuman, B.N.,  
667 Routson, C., 2021. A global Bayesian temperature calibration for lacustrine brGDGTs.  
668 *Geochim. Cosmochim. Acta* 305, 87–105. <https://doi.org/10.1016/j.gca.2021.04.038>
- 669 Peterse, F., van der Meer, J., Schouten, S., Weijers, J.W.H., Fierer, N., Jackson, R.B., Kim, J.-H.,  
670 Sinninghe Damsté, J.S., 2012. Revised calibration of the MBT–CBT paleotemperature  
671 proxy based on branched tetraether membrane lipids in surface soils. *Geochim.*

- 672 Cosmochim. Acta 96, 215–229. <https://doi.org/10.1016/j.gca.2012.08.011>
- 673 Raberg, J.H., Miller, G.H., Geirsdóttir, Á., Sepúlveda, J., 2023. Near-universal trends in  
674 brGDGT lipid distributions in nature. *Science Advances* 8, eabm7625.  
675 <https://doi.org/10.1126/sciadv.abm7625>
- 676 Rathburn, A.E., Willingham, J., Ziebis, W., Burkett, A.M., Corliss, B.H., 2018. A New  
677 Biological Proxy for Deep-Sea Paleo-Oxygen: Pores of Epifaunal Benthic Foraminifera.  
678 *Sci. Rep.* <https://doi.org/10.1038/s41598-018-27793-4>
- 679 Saravanan, P., Gupta, A.K., Zheng, H., Rai, S.K., Panigrahi, M.K., 2020. Changes in Deep-Sea  
680 Oxygenation in the Northeast Pacific Ocean During 32–10 ka. *Geophys. Res. Lett.* 47,  
681 e2019GL086613. <https://doi.org/10.1029/2019GL086613>
- 682 Schouten, S., Hopmans, E.C., Schefuss, E., Sinninghe Damsté, J.S., 2002. Distributional  
683 variations in marine crenarchaeotal membrane lipids: a new tool for reconstructing  
684 ancient sea water temperatures? *Earth Planet. Sci. Lett.* 204, 265–274.
- 685 Shipboard Scientific Party, 1992. Site 850, in: Pisias, N.G., Janecek, T.R., Baldauf, J.G.,  
686 Bloomer, S.F., Dadey, K.A., Emeis, K.-C., Farrell, J., Flores, J.A., Galimov, E.M.,  
687 Hagelberg, T.K., Holler, P., Hovan, S.A., Iwai, M., Kemp, A.E.S., Kim, D.C.,  
688 Klinkhammer, G., Leinen, M., Levi, S., Levitan, M.A., Lyle, M.W., MacKillop, A.K.,  
689 Meynadier, L.M., Mix, A.C., Moore, T.C., Raffi, I., Ravelo, C., Schneider, D.,  
690 Shackleton, N.J., Valet, J.-P., Vincent, E., Mayer, L.A., Pisias, N.G., Janecek, T.R.,  
691 Baldauf, J.G., Bloomer, S.F., Dadey, K.A., Emeis, K.-C., Farrell, J., Flores, J.A.,  
692 Galimov, E.M., Hagelberg, T.K., Holler, P., Hovan, S.A., Iwai, M., Kemp, A.E.S., Kim,  
693 D.C., Klinkhammer, G., Leinen, M., Levi, S., Levitan, M.A., Lyle, M.W., MacKillop,  
694 A.K., Meynadier, L.M., Mix, A.C., Moore, T.C., Raffi, I., Ravelo, C., Schneider, D.,  
695 Shackleton, N.J., Valet, J.-P., Vincent, E., Stewart, S.K., Kennett, D., Stewart, N.J.,  
696 Winkler, W.R. (Eds.), *Proceedings of the Ocean Drilling Program, 138 Initial Reports,*  
697 *Proceedings of the Ocean Drilling Program; Initial Reports; Part 1, Eastern Equatorial*  
698 *Pacific; Covering Leg 138 of the Cruises of the Drilling Vessel JOIDES Resolution,*  
699 *Balboa, Panama, to San Diego, California, Sites 844-854, 6 May 1991-5 July 1991.*  
700 *Ocean Drilling Program, Ocean Drilling Program, College Station, TX, United States, p.*  
701 *809.* <https://doi.org/10.2973/odp.proc.ir.138.115.1992>
- 702 Sinninghe Damsté, J.S., Hopmans, E.C., Pancost, R.D., Schouten, S., Geenevasen, J.A.J., 2000.  
703 Newly discovered non-isoprenoid glycerol dialkyl glycerol tetraether lipids in sediments.  
704 *Chem. Commun.* 1683–1684. <https://doi.org/10.1039/B004517I>
- 705 Studer, A.S., Mekik, F., Ren, H., Hain, M.P., Oleynik, S., Martínez-García, A., Haug, G.H.,  
706 Sigman, D.M., 2021. Ice Age-Holocene Similarity of Foraminifera-Bound Nitrogen  
707 Isotope Ratios in the Eastern Equatorial Pacific. *Paleoceanography and Paleoclimatology*  
708 36, e2020PA004063. <https://doi.org/10.1029/2020PA004063>
- 709 Tian, J., Fan, L., Liu, H., Liu, J., Li, Y., Qin, Q., Gong, Z., Chen, H., Sun, Z., Zou, L., Wang, X.,  
710 Xu, H., Bartlett, D., Wang, M., Zhang, Y.-Z., Zhang, X.-H., Zhang, C.L., 2018. A nearly  
711 uniform distributional pattern of heterotrophic bacteria in the Mariana Trench interior.  
712 *Deep Sea Res. Part I* 142, 116–126. <https://doi.org/10.1016/j.dsr.2018.10.002>
- 713 Tierney, J.E., Russell, J.M., 2009. Distributions of branched GDGTs in a tropical lake system:  
714 Implications for lacustrine application of the MBT/CBT paleoproxy. *Org. Geochem.* 40,  
715 1032–1036. <https://doi.org/10.1016/j.orggeochem.2009.04.014>
- 716 Tribouillard, N., Algeo, T.J., Lyons, T., Riboulleau, A., 2006. Trace metals as paleoredox and  
717 paleoproductivity proxies: An update. *Chem. Geol.* 232, 12–32.

- 718 <https://doi.org/10.1016/j.chemgeo.2006.02.012>  
719 Wang, X.T., Wang, Y., Auderset, A., Sigman, D.M., Ren, H., Martínez-García, A., Haug, G.H.,  
720 Su, Z., Zhang, Y.G., Rasmussen, B., Sessions, A.L., Fischer, W.W., 2022. Oceanic  
721 nutrient rise and the late Miocene inception of Pacific oxygen-deficient zones.  
722 *Proceedings of the National Academy of Sciences* 119, e2204986119.  
723 <https://doi.org/10.1073/pnas.2204986119>  
724 Weijers, J.W.H., Schouten, S., Hopmans, E.C., Geenevasen, J.A.J., David, O.R.P., Coleman,  
725 J.M., Pancost, R.D., Sinninghe Damsté, J.S., 2006a. Membrane lipids of mesophilic  
726 anaerobic bacteria thriving in peats have typical archaeal traits. *Environ. Microbiol.* 8,  
727 648–657. <https://doi.org/10.1111/j.1462-2920.2005.00941.x>  
728 Weijers, J.W.H., Schouten, S., Spaargaren, O.C., Sinninghe Damsté, J.S., 2006b. Occurrence and  
729 distribution of tetraether membrane lipids in soils: Implications for the use of the TEX86  
730 proxy and the BIT index. *Org. Geochem.* 37, 1680–1693.  
731 <https://doi.org/10.1016/j.orggeochem.2006.07.018>  
732 Weijers, J.W.H., Schouten, S., van den Donker, J.C., Hopmans, E.C., Sinninghe Damsté, J.S.,  
733 2007. Environmental controls on bacterial tetraether membrane lipid distribution in soils.  
734 *Geochim. Cosmochim. Acta* 71, 703–713. <https://doi.org/10.1016/j.gca.2006.10.003>  
735 Xie, S., Liu, X.-L., Schubotz, F., Wakeham, S.G., Hinrichs, K.-U., 2014. Distribution of glycerol  
736 ether lipids in the oxygen minimum zone of the Eastern Tropical North Pacific Ocean.  
737 *Org. Geochem.* 71, 60–71. <https://doi.org/10.1016/j.orggeochem.2014.04.006>  
738 Yin, S., Hernández-Molina, F.J., Jutzeler, M., Li, J., 2022. Progressive intensification of Pacific  
739 Deep Water circulation since the early Pliocene. *Geophys. Res. Lett.* 49.  
740 <https://doi.org/10.1029/2022gl098051>  
741 Zachos, J., Pagani, M., Sloan, L., Thomas, E., Billups, K., 2001. Trends, Rhythms, and  
742 Aberrations in Global Climate 65 Ma to Present. *Science* 292, 686–693.  
743 <https://doi.org/10.1126/science.1059412>  
744 Zell, C., Kim, J.-H., Moreira-Turcq, P., Abril, G., Hopmans, E.C., Bonnet, M.-P., Sobrinho,  
745 R.L., Damsté, J.S.S., 2013. Disentangling the origins of branched tetraether lipids and  
746 crenarchaeol in the lower Amazon River: Implications for GDGT-based proxies. *Limnol.*  
747 *Oceanogr.* 58, 343–353. <https://doi.org/10.4319/lo.2013.58.1.0343>  
748 Zeng, Z., Xiao, W., Zheng, F., Chen, Y., Zhu, Y., Zhang, C., 2023. Enhanced production of  
749 highly methylated brGDGTs linked to anaerobic bacteria from sediments of the Mariana  
750 Trench. *Frontiers in Marine Science* 10. <https://doi.org/10.3389/fmars.2023.1233560>  
751 Zhang, Y.G., Pagani, M., Liu, Z., 2014. A 12-Million-Year Temperature History of the Tropical  
752 Pacific Ocean. *Science* 344, 84–87. <https://doi.org/10.1126/science.1246172>  
753 Zhang, Y.G., Zhang, C.L., Liu, X.-L., Li, L., Hinrichs, K.-U., Noakes, J.E., 2011. Methane  
754 Index: a tetraether archaeal lipid biomarker indicator for detecting the instability of  
755 marine gas hydrates. *Earth Planet. Sci. Lett.* 307, 525–534.  
756 Zhou, X., Thomas, E., Rickaby, R.E.M., Winguth, A.M.E., Lu, Z., 2014. I/Ca evidence for upper  
757 ocean deoxygenation during the PETM. *Paleoceanography* 29, 964–975.  
758 <https://doi.org/10.1002/2014PA002702>